Electrical doping in halide perovskites

Julie Euvrard[1], Yanfa Yan[2] and David B. Mitzi[1,3]✉

Abstract | Electrical doping (that is, intentional engineering of carrier density) underlies most energy-related and optoelectronic semiconductor technologies. However, for the intensely studied halide perovskite family of semiconductors, reliable doping remains challenging, owing to, for example, compensation from and facile migration of intrinsic defects. In this Review, we first discuss the underlying fundamentals of semiconductor doping and then investigate different doping strategies in halide perovskites, including intrinsic defect, extrinsic defect and charge transfer doping, from an experimental as well as a theoretical perspective. We outline the advantages and pitfalls of different characterization techniques to assess doping and examine the impact of doping on optoelectronic properties. Finally, we highlight challenges that need to be overcome to gain control over the electronic properties of this important material class.

Halide perovskites (HaPs) are a broad class of materials adopting an ABX_3 crystal structure with corner-sharing BX_6 octahedra, analogous to the prototype $CaTiO_3$, but with a monovalent inorganic or organic A cation (for example, Cs^+ or $CH_3NH_3^+$), a divalent metal B cation (for example, Ge^{2+}, Sn^{2+} or Pb^{2+}) and an halide X anion (for example, Cl^-, Br^- or I^-). Lower-dimensional derivatives of this 3D structure have also been engineered, using partial or full substitution of the A site with larger organic cations, enabling layered (2D), chained (1D) and multidimensional perovskites with unprecedented leeway to tune physical properties[1,2]. With appropriate selection of constituents, these systems exhibit outstanding semiconducting properties (for example, tunable direct bandgap, electronically benign defects and strong optical absorption) and form the basis for a variety of devices, including solar cells[3–5], photodetectors[6,7], transistors[8,9], light-emitting diodes[10,11], lasers[12,13] and thermoelectric generators[14]. Notably, Pb-based HaPs have enabled unprecedented advancement in perovskite solar cell performance, with power conversion efficiencies (PCEs) reaching 25.2% in ~10 years of development[15]. In contrast to traditional inorganic electronics, such as Si-based or GaAs-based electronics, HaPs can be made mechanically flexible and semi-transparent, and they allow large-area solution processing at low cost[16–18]. Nevertheless, despite impressive technological progress, a basic understanding and control of the underlying properties of these materials remain limited[19,20].

Our ability to master semiconductor technology depends on control over the type (p or n) and density of electrical carriers (electrons or holes) in the design of optimized devices[21]. The term 'doping' is broadly used in HaP literature to describe the introduction of any kind of impurity into the lattice to control crystal growth and stability or to tune optoelectronic properties[22,23]. In this Review, we focus on electrical doping, that is, the introduction of an impurity or defect to generate free carriers or to shift the Fermi level. Doping for the generation of free carriers has enabled the rise of microelectronics, with the formation of p–n junctions and improved contact quality between the semiconductor and the electrodes. Crystalline Si, Ge and GaAs exhibit excellent ambipolar doping with carrier densities of up to 10^{18}–10^{20} cm^{-3} (REFS[21,24]), whereas most other semiconductors present preferred n-dopability or p-dopability with variable effectiveness[24]. Considerations of HaP doping have been explored early on with the observation that Sn-based perovskites have p-type semimetallic properties and can be tuned upon Sn oxidation[25–30]. However, efficient and reliable tuning of carrier density remains particularly challenging in HaPs, because major difficulties have arisen, including compensation from intrinsic defects.

Different strategies have been explored for HaP doping, which can be categorized into intrinsic defect doping, extrinsic defect doping and charge transfer doping. Intrinsic and extrinsic (impurity) doping rely on the formation of charged defects in the lattice structure. Charge transfer doping occurs through exchange of carriers between the perovskite semiconductor and an external entity, such as a molecule or interface. In this Review, we first briefly address the fundamentals of electrical doping in semiconductors, and then examine theoretical and experimental studies on HaP doping. Approaches used to assess doping further play an important role in the conclusions drawn for perovskite doping studies, and, therefore, we also discuss the features and pitfalls of different characterization techniques. Finally, we discuss doping in the context of device engineering and highlight the central question of dopability (that is, the ability to generate free carriers). Of note, although we

[1]Department of Mechanical Engineering and Materials Science, Duke University, Durham, NC, USA.

[2]Department of Physics and Astronomy, and Wright Center for Photovoltaic Innovation and Commercialization, The University of Toledo, Toledo, OH, USA.

[3]Department of Chemistry, Duke University, Durham, NC, USA.

✉e-mail: david.mitzi@duke.edu

https://doi.org/10.1038/s41578-021-00286-z

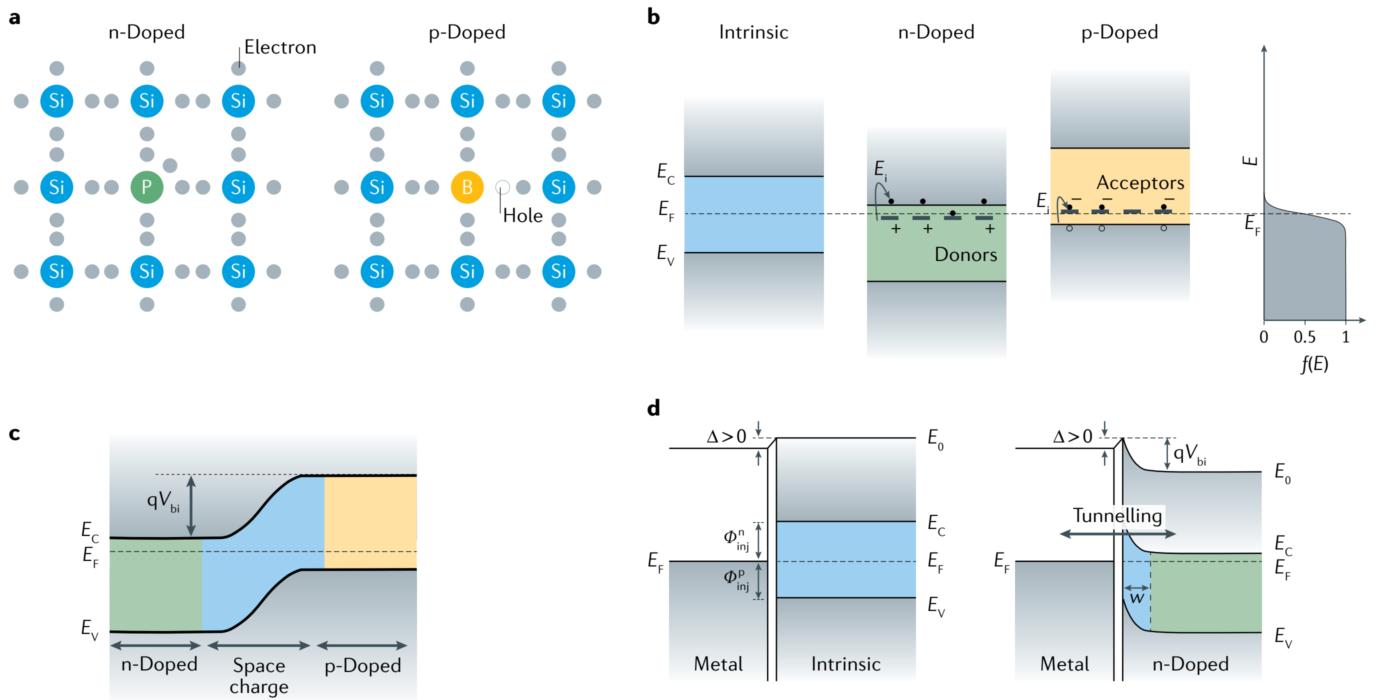

Fig. 1 | **n-Doping and p-doping in silicon and impact on interfaces. a** | Schematic view of bond formation in silicon, n-doped and p-doped with phosphorous (P) and boron (B) impurities, respectively. **b** | Formation of donor and acceptor levels with ionization energy E_i and shift of the Fermi level E_F towards the conduction band minimum (CBM) and valence band maximum (VBM) for n-type and p-type doping, respectively. $f(E)$ corresponds to the Fermi–Dirac distribution and E is the energy with respect to the vacuum level. E_C and E_V are the energies of the CBM and VBM, respectively. **c** | Schematic of a p–n homojunction with formation of a space charge region and built-in potential V_{bi}. The presence of band bending implies an electric field in this region of the semiconductor. q is the elementary charge. **d** | Energy level diagram for a metal–semiconductor interface with a dipole Δ considering an intrinsic and an n-doped semiconductor. The space charge region exhibits a thickness w and a built-in potential V_{bi}. Φ^{n}_{inj} and Φ^{p}_{inj} are the electron and hole injection barriers, respectively, and E_0 is the vacuum level.

focus on 3D perovskite systems, the same concepts also apply to lower-dimensional systems.

Fundamentals of electrical doping

Electrical doping of a semiconductor implies the addition of extra electrons (or holes) in the conduction (or valence) band to generate additional mobile carriers. In intrinsic semiconductors, the electron n and hole p densities balance[31]:

$$n = p = n_i = \sqrt{N_C N_V}\exp\left(-\frac{E_G}{2k_B T}\right) \quad (1)$$

where N_C and N_V are the effective densities of states in the conduction and valence bands, respectively (dependent on effective masses and temperature), E_G is the semiconductor bandgap, k_B is the Boltzmann constant and T the temperature. Electrical doping relies on the formation of intrinsic (vacancies, interstitials or site substitutions) and/or extrinsic (impurities) defects[32]. An example of an extrinsic defect is P (P_{Si}) and B (B_{Si}) substituted in silicon for n-type and p-type doping, respectively (FIG. 1a). P and B have a different number of valence electrons compared with the substituted host, which leads to the creation of extra carriers upon defect ionization. Qualitatively, n-type and p-type dopants generate donor levels (E_D) below the conduction band minimum (CBM) and acceptor levels (E_A) above the valence band maximum (VBM), respectively (FIG. 1b). The distance between the band edge and the dopant level, also called the transition energy, determines the rate of impurity ionization. A sufficiently small transition energy, for example, within a few tens of meV, ensures complete impurity ionization at room temperature. Upon doping, the Fermi level, E_F, defined at 50% probability of electron occupancy ($f(E_F) = 0.5$) using the Fermi–Dirac distribution $f(E)$[31]:

$$f(E) = \frac{1}{1 + \exp\left(\frac{E - E_F}{k_B T}\right)} \quad (2)$$

shifts towards the CBM for n-type doping and towards the VBM for p-type doping (FIG. 1b). Therefore, Fermi–Dirac statistics define n and p in a semiconductor under thermal equilibrium conditions[31]:

$$n = N_C \exp\left(-\frac{E_C - E_F}{k_B T}\right) \quad (3)$$

$$p = N_V \exp\left(-\frac{E_F - E_V}{k_B T}\right) \quad (4)$$

where E_C and E_V are the energies of the CBM and VBM, respectively. Upon high-level doping, E_F may cross the band edge, leading to a degenerate semiconductor with essentially metallic properties. Although usually used to achieve higher electron or hole densities, doping can also be applied to compensate carrier concentrations (that is, to reduce carrier density or change the majority carrier type).

The ability to tune the Fermi level position provides the foundation for the engineering of efficient electronic devices. For example, n-doped and p-doped Si layers can be brought into contact to form the widely used p–n homojunction (FIG. 1c). Owing to electron and hole density gradients, mobile electrons (or holes) diffuse from the n-type (or p-type) into the p-type (or n-type) region and recombine as minority carriers within approximately a diffusion length of the junction. Ionized impurities at the junctions are not compensated by mobile carriers and, thus, form a depletion or space charge region. Thermal equilibrium is achieved when the electric field in the space charge region balances the diffusion process. In a p–n junction, the built-in voltage V_{bi} is given by the difference between the Fermi energies in the n-doped ($E_{F,n}$) and the p-doped ($E_{F,p}$) regions: $qV_{bi} = E_{F,n} - E_{F,p}$, where $E_{F,n}$ and $E_{F,p}$ are defined relative to a universal 'vacuum' energy level and q is the elementary charge[33]. Therefore, strong doping increases E_F shifts and V_{bi}. A metal–semiconductor interface can be compared with a p–n junction, with one of the semiconductor layers being degenerately doped (FIG. 1d). The space charge region extends exclusively in the semiconductor layer and the depletion width w of the space charge region decreases with increasing donor N_D and acceptor N_A densities for n-doped and p-doped semiconductors, respectively[33]:

$$w = \sqrt{\frac{2\varepsilon_r \varepsilon_0 V_{bi}}{qN_{D/A}}}, \quad (5)$$

where ε_r is the relative permittivity of the semiconductor and ε_0 the vacuum permittivity. At high doping concentrations, band bending becomes sufficiently strong and depletion width sufficiently thin (a few nm) to allow charge injection and extraction by tunnelling through prospective interfacial barriers. Strong contact doping is widely used in microelectronics to transform a Schottky contact (FIG. 1d), in which carriers need to be thermally activated to overcome the electron Φ_{inj}^{n} or hole Φ_{inj}^{p} injection barriers, to a quasi-ohmic contact for one type of carrier, thereby, addressing the key challenge of achieving effective electrical connection with the device.

Beyond interface engineering, electrical doping modifies critical transport properties. For example, the conductivities of electrons (or holes), $\sigma_n = qn\mu_n$ (or $\sigma_p = qp\mu_p$), depend on the carrier densities n/p and mobilities μ_n/μ_p. Therefore, conductivity measurements are often used to probe semiconductor doping. Importantly, conductivity increase does not necessarily imply electrical doping and E_F shift, because an increase in mobility can also underlie this change. The effective semiconductor mobility μ_{eff} is limited by different scattering mechanisms and can be approximated by the Matthiessen's rule[34]:

$$\frac{1}{\mu_{eff}} = \frac{1}{\mu_{impurity}} + \frac{1}{\mu_{phonon}} + \frac{1}{\mu_{defect}} \quad (6)$$

where $\mu_{impurity}$, μ_{phonon} and μ_{defect} are individual mobilities, limited by coulombic interactions with impurities, phonon scattering with the lattice and surface or bulk defects, respectively. The introduction of carriers and ionized impurities may impact μ_{eff} through changes in the different scattering mechanisms.

Moreover, recombination mechanisms are influenced by doping. The generation and recombination dynamics of charge carriers in semiconductors are usually described by (using electron density as an example)[35]:

$$\frac{dn}{dt} = G - k_1 n - k_2 n^2 - k_3 n^3 \quad (7)$$

where G ($cm^{-3} s^{-1}$) is the generation rate and k_1 (s^{-1}), k_2 ($cm^3 s^{-1}$) and k_3 ($cm^6 s^{-1}$)are monomolecular (typically related to charge trapping), bimolecular (electron–hole recombination) and Auger recombination rates, respectively. k_2 and k_3 are intrinsic parameters for a given semiconductor, and k_1 is extrinsic and evolves with defect and doping density[36].

Doping in halide perovskites

Different strategies have been explored to tune the carrier concentration and E_F position in HaPs. Electrical doping is usually achieved through defect formation to provide extra electrons or holes to the lattice. Intrinsic defects can be engineered by changing the constituent chemical potentials or the precursor ratio during synthesis, and extrinsic defects can be generated by introducing impurity atoms in the crystal structure. Alternatively, charge transfer doping takes advantage of the substrate work function or strong molecular acceptors or donors to induce charge transfer.

Intrinsic defect doping. Electrical doping can be achieved by introducing intrinsic defects in the ABX_3 crystal lattice (FIG. 2a), namely, vacancies (V_A, V_B, V_X), interstitials (A_i, B_i, X_i) and substitutions (A_B, B_A, A_X, X_A, B_X, X_B). Density functional theory (DFT) calculations are useful for predicting E_F tuning as a result of defect formation[37–42], with the calculated transition energy of each defect marking the position of the state (E_D or E_A) within the bandgap, for example, in $MAPbI_3$ (where MA is methylammonium)[37] (FIG. 2b). Notably, many defects in $MAPbI_3$ are shallow (close to VBM or CBM); shallow defects ionize more easily at room temperature and act as efficient dopants. The carrier density or E_F is determined by the difference between shallow donor and acceptor defect densities. Typically, the carrier density in a semiconductor is limited by two major factors: the ability to incorporate sufficient dopant density within the structure and heavy compensation, that is, dopants incorporated with only a small difference in donor and acceptor densities. Under thermal equilibrium growth

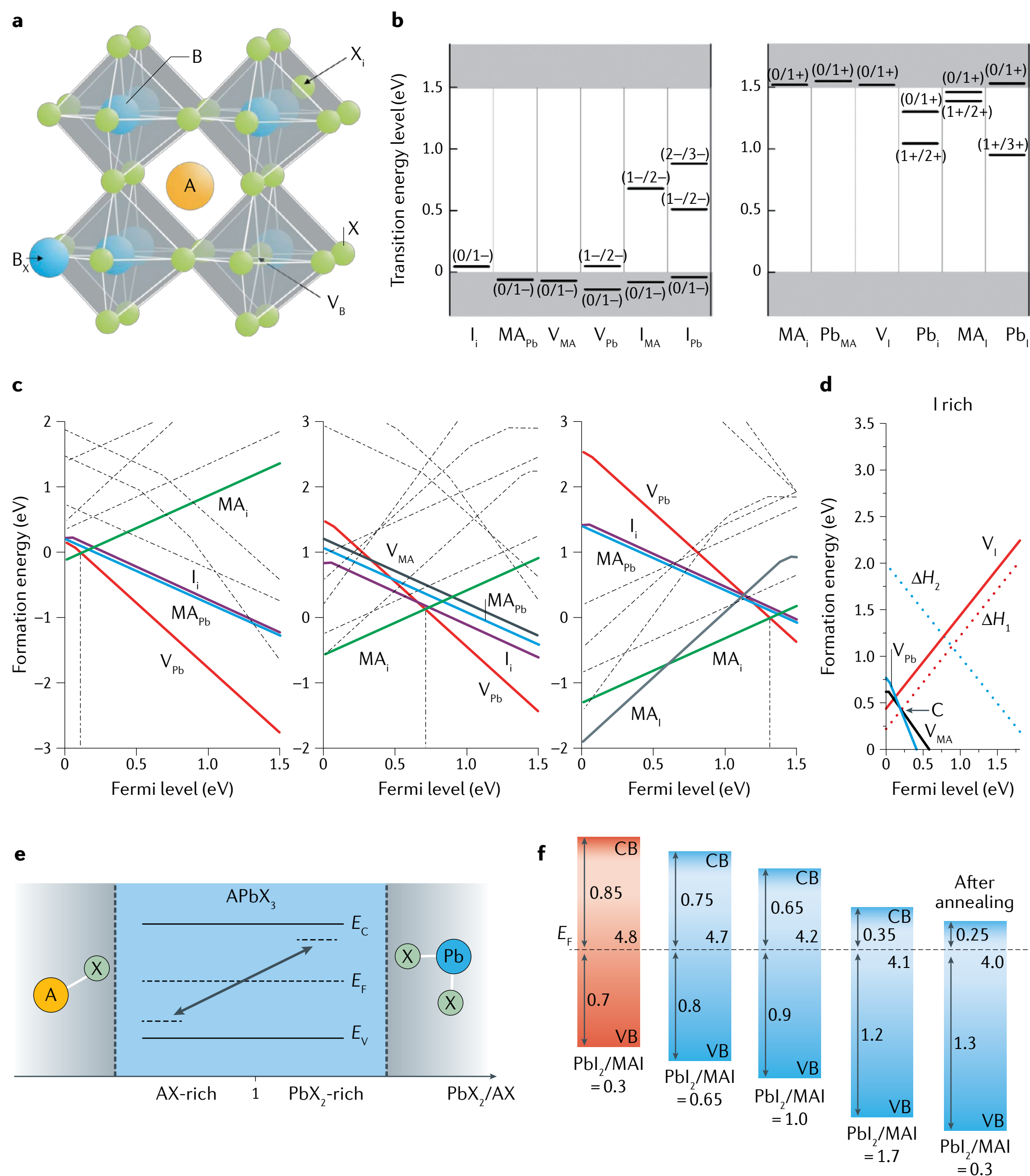

conditions, the density of a particular defect α ionized to the charge state q depends on its formation energy $\Delta H(\alpha, \mathrm{q})$, which can be calculated by[38]:

$$\Delta H^{(\alpha,\mathrm{q})}(\mu_i, E_\mathrm{F}) = \Delta H^{(\alpha,\mathrm{q})}(0,0) + \sum_i n_i\mu_i + \mathrm{q}E_\mathrm{F} \quad (8)$$

where $\Delta H^{(\alpha,\mathrm{q})}(0{,}0)$ is the defect formation energy for $\mu_i = 0$, $E_\mathrm{F} = 0$, $\sum_i n_i\mu_i$ is the sum of the chemical potentials of the constituent elements (with n_i the number of element i) and E_F the Fermi energy referenced to the VBM. The growth conditions have an impact on the chemical potentials μ_i and, therefore, on the defect formation energy. Typically, defect formation energies $\Delta H_\mathrm{f}(\alpha,\mathrm{q})$ are calculated as a function of E_F for specific chemical potentials, which are constrained by secondary phase formation. Notably, the above calculations are based on bulk materials under thermal equilibrium growth conditions. The growth of nanocrystals can be affected by kinetic factors and high surface-to-volume ratios, which make the accurate calculation of defect energies in these systems challenging.

The defect formation energies for $MAPbI_3$ can be calculated for different chemical potential conditions, such as I-rich and Pb-poor, moderate or I-poor and Pb-rich[37] (FIG. 2c). The position of E_F in $MAPbI_3$ is pinned by compensation among dominant donors and acceptors, that is, MA_i and V_{Pb} (vertical dashed lines in FIG. 2c), for which formation energies depend on the constituent chemical potentials. Accordingly, ambipolar doping is predicted for $MAPbI_3$, depending on growth conditions[37], a trend also observed in $FAPbI_3$ (where FA is formamidinium)[43]. Interestingly, similar calculations for $MAPbBr_3$ show a predominantly unipolar self-doping character[39], with a tuning range from degenerately p-doped under Br-rich and Pb-poor condition to intrinsic or slightly n-doped in

◀ Fig. 2 | **Halide perovskite doping through precursor ratio variations. a** | Schematic view of substitutional (B_X), vacancy (V_B) and interstitial (X_i) intrinsic defects in an ABX_3 perovskite crystal lattice. **b** | Calculated intrinsic acceptor (left) and donor (right) transition energy levels for $MAPbI_3$ (where MA is methylammonium) (charge state transition specified in parentheses)[37]. **c** | Formation energies of intrinsic point defects in $MAPbI_3$ calculated in I-rich and Pb-poor (left), moderate (middle) and I-poor and Pb-rich (right) conditions[37]. The Fermi level is given with respect to the valence band maximum (VBM). Defects with high formation energies are displayed as dashed lines. **d** | Calculated vacancy defect and thermally excited band-edge states (to account for free carriers) formation energies as functions of the Fermi level (given with respect to the VBM) for $MAPbI_3$ at $T = 300$ K in I-rich conditions[44]. Vacancy defects (V_{MA}, V_I and V_{Pb}) and thermally excited band-edge states (ΔH_1 and ΔH_2) formation energies are displayed as solid and dashed lines, respectively. The Fermi level (point C) is pinned by V_{Pb} and band-edge states. **e** | Schematic view of the Fermi level E_F evolution in $APbX_3$ perovskite structures, if the PbX_2/AX ratio is tuned from AX-rich to PbX_2-rich conditions. The existence of $APbX_3$ is constrained by the formation of secondary phases (AX and PbX_2). E_C and E_V are the conduction band minimum and VBM energies, respectively. **f** | Energetic levels obtained by ultraviolet photoelectron microscopy for $MAPbI_3$ synthesized with varying PbI_2/MAI ratio and for PbI_2/MAI = 0.3 after annealing at 150 °C for 45 min (REF.[46]). CB and VB correspond to the conduction band and valence band, respectively. Panels **b** and **c** are reprinted from REF.[37], with the permission of AIP Publishing. Panel **d** is adapted from REF.[44], CC BY 4.0 (https://creativecommons.org/licenses/by/4.0/). Panel **f** is reprinted from REF.[46], with the permission of AIP Publishing.

Br-poor and Pb-rich condition. These theoretical calculations suggest the importance of compensation in HaPs, as well as the possibility of significant doping by intrinsic defect concentrations and different growth conditions. In addition to intrinsic defects, free carriers may have an impact on E_F pinning, which are generally omitted in DFT calculations[44]. For $MAPbI_3$, the impact of free holes associated with thermally excited band-edge donors (ΔH_1) dominates over Schottky defects at room temperature, pinning E_F at ~180 meV above the VBM (FIG. 2d). However, it remains unclear how thermal band-edge excitations, which become dominant for a high density of free carriers[44], limit the E_F tuning range in HaPs.

DFT calculations performed on the Sn-based perovskites $CsSnI_3$, $FASnI_3$ and $MASnI_3$ show high-level p-doping, owing to V_{Sn} stability under I-rich and Sn-poor conditions[38,40,41]. Computational modelling points to the possibility of mitigating (if necessary) strong p-doping by using Sn-rich growth conditions. For example, a decrease from 10^{19} cm^{-3} to 10^{15} cm^{-3} is predicted for the hole density in $MASnI_3$, which remains p-type under all proposed growth conditions[41]. Owing to a higher formation energy of V_{Sn} in $FASnI_3$ and $CsSnI_3$, these compounds are predicted to achieve intrinsic or weakly n-type properties in a Sn-rich growth condition[38,40]. Notably, DFT calculation accuracy can be limited by a variety of factors, including exchange–correlation functionals, supercell size and secondary phase constraints[45]. For example, the use of a hybrid functional with an optimized mixing parameter and inclusion of spin–orbit coupling (SOC) is necessary to correctly predict Pb-based HaP bandgaps. In addition, challenges remain to employ these computational approaches for defect calculations, because large supercell sizes are necessary to avoid defect–defect interaction. Most defect calculations do not consider hybrid functional and SOC. Therefore, although DFT calculations are useful for qualitatively determining the compositional limits achievable for a given material under thermodynamic equilibrium growth conditions, the predictions should be experimentally verified.

Intrinsic defects for the doping of HaPs can be experimentally realized by tuning the precursor ratio during film deposition from solution[46–48] and evaporation[49], or post deposition through thermal treatments[50–52]. Notably, precursor ratio variations do not directly relate to changes in constituent chemical potentials as typically considered in DFT studies, because synthetic studies involve addition or subtraction of a salt, rather than individual atoms. Experimental studies show qualitative agreement with theoretical calculations, with tunable carrier density and type being achieved through variations in the PbX_2/AX ratio in the $APbX_3$ structure[46–49,53] (FIG. 2e, TABLE 1). A transition from p-type to n-type has been reported in $MAPbI_3$, with a ~500-meV E_F up-shift upon varying the PbI_2/MAI ratio from 0.3 (Pb-poor) to 1.7 (Pb-rich) in the precursor solution[46,47] (FIG. 2f); similar behaviour has been reported for $FAPbI_3$ (REF.[47]). Hall effect measurements showed a large change in carrier density from $p = 4.0 \times 10^{16}$ cm^{-3} (p-type) to $n = 3.5 \times 10^{18}$ cm^{-3} (n-type) over a PbI_2/MAI ratio range of 0.3 to 1.7 (REF.[46]); however, such high doping levels have not been confirmed in subsequent studies, which, rather, point to a general limitation of carrier densities at $<10^{14}$ cm^{-3} for $MAPbI_3$ (TABLE 1). The E_F positions of these $MAPbI_3$ samples can be extracted using ultraviolet photoelectron spectroscopy[46]; applying Fermi–Dirac statistics (Eq. (3)) to these results with $N_C = 1.44 \times 10^{18}$ cm^{-3} (REF.[54]) implies a maximum carrier density of $n = 2 \times 10^{12}$ cm^{-3}, which is in good agreement with values reported for $MAPbI_3$ obtained in stoichiometric and non-stoichiometric conditions[48,52,53,55].

A similar transition from p-type to n-type with increasing $PbBr_2$/MABr ratio has been observed in $MAPbBr_3$ single crystals[56]. However, close to intrinsic carrier densities of ~10^7 cm^{-3} for both p-type (Pb-poor) and n-type (Pb-rich) suggest, pending further confirming studies, a limited doping range achievable through precursor ratio variations for X=Br. These experimental observations contrast with theoretical calculations, which suggest the possibility of a degenerate p-type doping behaviour at Pb-poor conditions for $MAPbBr_3$ (REF.[39]). As an alternative to precursor ratio variation during deposition, post-deposition thermal treatments have been used to tune intrinsic point defects; for example, a 550-meV E_F shift towards the CBM has been reported following a 160 °C annealing treatment, changing the $MAPbI_3$ layer from p-type to n-type as volatile MAI dissociates from the film during annealing[51]. Post-deposition annealing under I_2 atmosphere further leads to a 150-meV E_F shift towards the VBM, therefore, acting as p-dopant[52]. The p-doping effect can be attributed to a decrease in donor defect density V_I or to defect complexes containing V_I when exposed to I_2 vapour. Non-intentional field and photoinduced doping owing to local accumulation of defects have also been reported and attributed to ion motion and photolysis, respectively, which may be particularly important for HaPs (that is, doping levels may change with time and depend on electrical fields, concentration gradients and lighting)[57,58].

Table 1 | **Doping densities and Fermi level position achieved by precursor ratio variation**

Compound and processing	Type	*n* (cm^{-3})	*p* (cm^{-3})	$E_C - E_F$ (meV)	$E_F - E_V$ (meV)	Technique	Ref.
$MAPbI_3$							
$MAPbI_3$	p	–	7.6×10^{10}	–	–	Hall (CRPH)	137
$PbI_2/MAI = 0.3$	p	–	4.0×10^{16}	–	700	Hall; UPS	46
$PbI_2/MAI = 1.7$	n	3.5×10^{18}	–	350	–		
No annealing	p	–	6.3×10^{16}	–	550	Capacitance; XPS	51
160 °C	n	5.0×10^{17}	–	400	–		
No annealing	p	–	$\sim 10^{12}$	–	600	Conductivity; UPS	52
Annealing in I_2 vapour	p	–	$\sim 9 \times 10^{12}$	–	450		
No annealing	p	–	$\sim 2 \times 10^{11}$	–	550	Hall; XPS	194
150 °C	n	$\sim 10^{11}$	–	530	–		
$PbI_2/MAI = 0.3$	p	–	–	–	680	STS	47
$PbI_2/MAI = 1.7$	n	–	–	390	–		
$PbI_2/MAI = 0.91$	p	–	$\sim 8 \times 10^{9}$	–	500	Hall; XPS	53
$PbI_2/MAI = 1.1$	n	$\sim 4 \times 10^{12}$	–	320	–		
$PbI_2/MAI = 1$	n	1.3×10^{11}	–	–	–	Hall (CRPH)	48
$PbI_2/MAI = 1.05$	n	2.7×10^{12}	–	–	–		
$MAPbI_3$ (polycrystalline)	n	1.5×10^{9}	–	–	–	Hall	195
$MAPbBr_3$							
$PbBr_2/MABr = 0.2$	p	–	1.3×10^{7}	–	–	Hall	56
$PbBr_2/MABr = 1.5$	n	4.9×10^{7}	–	–	–		
$MAPbBr_3$	p	–	$\sim 2 \times 10^{7}$	–	–	Hall	196
$MAPbBr_{2.94}Cl_{0.06}$	i	$\sim 5 \times 10^{6}$	$\sim 5 \times 10^{6}$	–	–		
$MAPbCl_3$	n	$\sim 2 \times 10^{8}$	–	–	–		
$FAPbI_3$							
$PbI_2/FAI = 0.3$	p	–	–	–	570	STS	47
$PbI_2/FAI = 1.7$	n	–	–	410	–		
$(FA,MA)Pb(I,Br)_3$							
$(FAPbI_3)_{0.88}(MAPbBr_3)_{0.12}$	p	–	8.3×10^{11}	–	–	Hall (CRPH)	137
$MASnI_3$							
$MASnI_3$	p	–	2.0×10^{19}	–	–	Hall	25
$MASnI_3$ (single crystals)	p	–	$\sim 10^{11}$	–	–	Hall	197
$MASnI_3$ (polycrystalline)	n	9.1×10^{13}	–	–	–	Hall	195
$MASnI_3$ (polycrystalline, open tube method)	p	–	7.9×10^{14}	–	–		
$FASnI_3$							
0 mol% SnF_2	p	–	2.2×10^{20}	–	–	OPTPS	63
10 mol% SnF_2	p	–	7.2×10^{18}	–	–		
0 mol% SnF_2	p	–	3×10^{19}	–	–	Capacitance	67
15 mol% SnF_2	p	–	1.1×10^{17}	–	–		
$FASnI_3$ (single crystals)	n	$\sim 10^{11}$	–	–	–	Hall	197
$FASnI_3$ (polycrystalline)	n	8.4×10^{13}	–	–	–	Hall	195
$CsSnI_3$							
0 mol% SnF_2	p	–	$\sim 10^{19}$	–	–	Hall	66
20 mol% SnF_2	p	–	$\sim 10^{17}$	–	–		
0 mol% SnF_2	p	–	$>5.7 \times 10^{17}$	–	–	TA	68
20 mol% SnF_2	p	–	$\sim 2.8 \times 10^{16}$	–	–		
$CsSnI_3$ (polycrystalline)	n	8.7×10^{14}	–	–	–	Hall	195

Table 1 (cont.) | **Doping densities and Fermi level position achieved by precursor ratio variation**

Compound and processing	Type	n (cm^{-3})	p (cm^{-3})	$E_C - E_F$ (meV)	$E_F - E_V$ (meV)	Technique	Ref.
$CsSnBr_3$							
0 mol% SnF_2	n	–	–	50	–	UPS	64
20 mol% SnF_2	n	–	–	150	–		
$CsSnBr_3$ (single crystal, solution-grown)	p	–	7.5×10^{16}	–	–	Hall	131
$CsSnBr_3$ (single crystal, melt-grown)	p	–	6.2×10^{15}	–	–		

The table displays the type (p or n), electron density n, hole density p, difference between the conduction band minimum energy E_C and the Fermi level E_F ($E_C - E_F$), difference between E_F and the VBM energy E_V ($E_F - E_V$) and the analysis technique used for each study. CRPH, carrier-resolved photo-Hall; OPTPS, optical-pump THz-probe spectroscopy; STS, scanning tunnelling spectroscopy; TA, transient absorption spectroscopy; UPS, ultraviolet photoelectron spectroscopy; XPS, X-ray photoelectron spectroscopy.

Experimental Sn-based perovskite studies are qualitatively consistent with theoretical predictions. Strong p-doping is generally observed in $ASnX_3$ systems and attributed to the oxidation of Sn^{2+} to Sn^{4+} and to the facile formation of V_{Sn} during synthesis or through degradation processes[25,28–30,59–62]. As suggested by theory[38,40,41], V_{Sn} can be altered in Sn-rich growth conditions, usually achieved by adding extra SnF_2 in the precursor solution[63–69]. The presence of Sn salts in excess in the precursor solution, which, presumably, do not incorporate into the perovskite crystal structure itself[66,68], may increase the V_{Sn} formation energy, thereby, reducing the background hole density; for example, a hole density decrease from 2.2×10^{20} cm^{-3} to 7.2×10^{18} cm^{-3} with 10 mol% added SnF_2 (with respect to SnI_2) has been reported in $FASnI_3$ (REF.[63]). The doping compensation with SnF_2 decreases the recombination rate and improves carrier mobility from 23 cm^2 V^{-1} s^{-1} to 67 cm^2 V^{-1} s^{-1} through a reduction of ionized acceptor scattering. Nevertheless, the intrinsic properties of $FASnI_3$ suggested by DFT have not yet been experimentally achieved[40]. Additional details on the effects of SnF_2 addition in Sn-based systems can be found elsewhere[65].

Extrinsic defect doping. The dopability of $MAPbI_3$ has been explored with various impurity atoms in DFT calculations[70] (FIG. 3a). As for intrinsic defect calculations, the selection of functional, SOC, supercell size and possible secondary phases may affect the accuracy of the predictions for extrinsic defect doping. Although many impurities produce shallow donors or acceptors, dopability is typically limited by compensation involving intrinsic defects (such as V_{Pb}, V_I, I_i, MA_I and MA_i). Therefore, the formation energy of both extrinsic and intrinsic defects has been calculated for $MAPbI_3$ under various growth conditions[70]. From DFT calculations, degenerate p-type doping is expected upon Pb substitution with Na or K (Na_{Pb}, K_{Pb}) and I substitution with O (O_I) in I-rich and Pb-poor growth conditions, whereas limited n-type doping has been suggested in I-poor and Pb-rich conditions. However, extrinsic dopants cannot achieve n-type doping beyond what can be realized with intrinsic defects, highlighting the importance of charge compensation in HaPs and that careful control of growth conditions may favour more efficient extrinsic doping. Extrinsic defects have also been studied in $MAPbBr_3$ using DFT, with the particular objective to alter the unipolar p-type character of this compound[39]. Nevertheless, none of the impurities considered could achieve n-type doping, owing to heavy compensation from intrinsic defects, such as V_{Pb} and V_{Br}. In $CsPbI_3$, In_{Pb} and Tl_{Pb} have been suggested to induce p-type doping, whereas Sb_{Pb} and Bi_{Pb} result in n-type doping[71]. However, intrinsic defect formation has not been considered, and, thus, the contribution of charge compensation from intrinsic defects remains elusive.

Impurity doping in HaPs has also been experimentally demonstrated (TABLE 2). Although not intentionally introduced in the structure, oxygen adsorption and dissolution can serve as acceptor, which causes ‘dedoping’ of initially n-type $MAPbI_3$, with a ~500-meV E_F down-shift[72]. Moreover, oxygen exposure is shown to increase the conductivity by an order of magnitude for a supposedly p-type $MAPbI_3$ (REF.[73]). A conversion from n-type to p-type $MAPbI_3$ has also been observed upon NaI and RbI addition in solution[74,75], consistent with DFT calculations[70] and pending further confirming experimental studies. Moreover, the incorporation of the monovalent cations Cu^+, Na^+ and Ag^+ in $MAPbI_3$, with concentrations of ~1–2 mol%, improve solar cell PCE and lead to a ~100-meV work function (W_f) shift towards the VBM, attributed to surface passivation[76]. Although Cu_i is expected to be an n-type dopant[70], ultraviolet photoelectron spectroscopy measurements have shown a 760-meV E_F shift towards the VBM in $MAPbI_3$ with a CuSCN additive (of note, X-ray photoelectron spectroscopy suggests that the I and Pb peaks shift towards higher binding energies)[77].

Sb^{3+} and Bi^{3+} doping has also generated interest, although DFT calculations suggest that it is not promising for $MAPb(I,Br)_3$, owing to large formation energies and compensation from intrinsic defects[39,70,78]. Hall effect measurements showed that the electron density increases from 7.2×10^{14} cm^{-3} to 8.3×10^{16} cm^{-3} for undoped and 2% Sb-doped $MAPbI_3$ (REF.[79]), respectively. However, ultraviolet photoelectron spectroscopy and scanning tunnelling spectroscopy measurements reveal only a weak E_F shift towards the CBM, implying a shift of the semiconductor from intrinsic or slightly p-type to weakly n-type[79,80]. Moreover, it is unclear whether the introduction of Sb impurities influences the MAI/PbI_2 ratio during film formation, which may subsequently impact doping. A ~300-meV

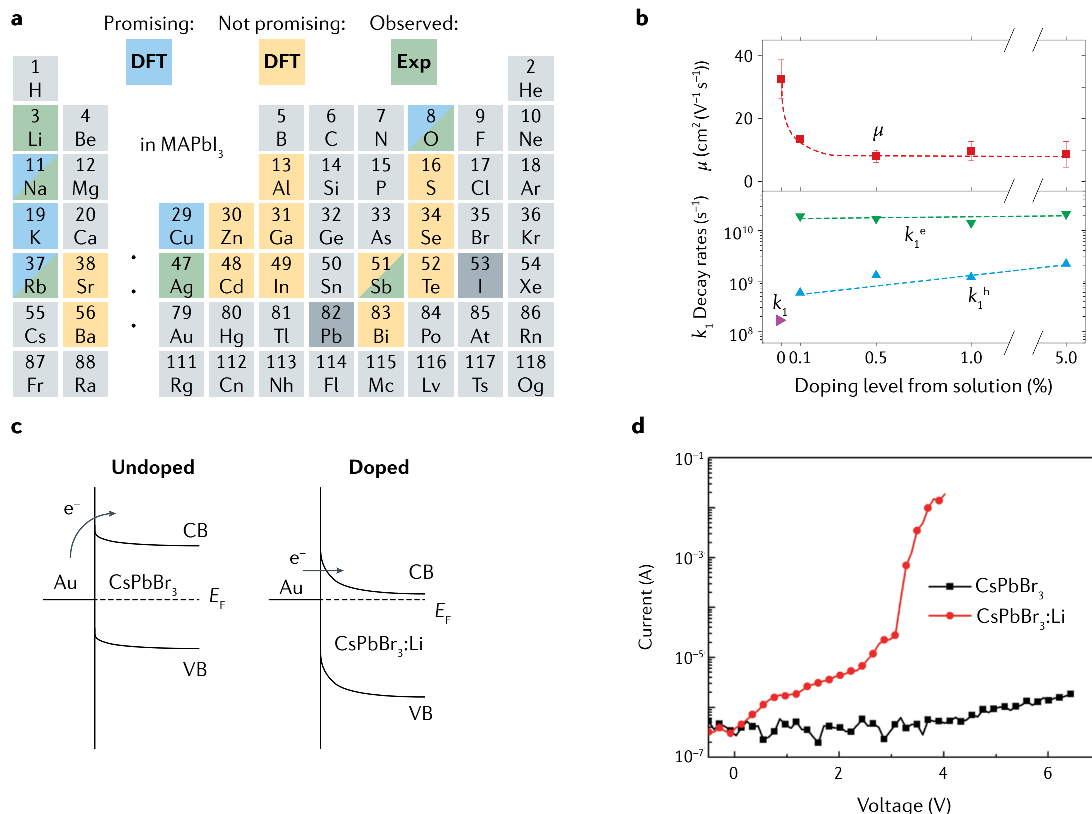

Fig. 3 | **Halide perovskite doping with substitutional and interstitial impurities. a** | Truncated periodic table of elements summarizing density functional theory (DFT) and experimental (Exp) studies on $MAPbI_3$ (where MA is methylammonium) doping with impurities[70,74,75,79,90,94]. DFT results suggesting an impact of the impurity on the Fermi level E_F are blue (promising), whereas yellow (not promising) represents impurities that should have no impact on the E_F position. **b** | Electron–hole sum mobility μ (red squares) and monomolecular decay rates k_1 extracted from optical-pump THz-probe (OPTP) measurements for undoped and Bi^{3+}-doped $MAPbBr_3$ (REF.[87]). A single value of k_1 (magenta right-pointing triangle) was extracted for electrons and holes in the undoped sample. For doped samples, decay rates k_1^e (green down-pointing triangles) and k_1^h (blue up-pointing triangles) were extracted and assigned to initial fast trapping of electrons and slow decay of the photoexcited hole population, respectively. **c** | Energy band diagram at the Au–perovskite interface at zero bias. **d** | Current–voltage (I–V) characteristics of light-emitting diodes without (black) and with (red) a Li^+-doped $CsPbBr_3$ hole transport layer[95]. E_F, CB and VB correspond to the Fermi energy, conduction band and valence band, respectively. Panel **b** is adapted with permission from REF.[87], American Chemical Society. Panels **c** and **d** are reprinted with permission from REF.[95], American Chemical Society.

bandgap narrowing and a carrier density increase from ~6×10^9 cm^{-3} to ~10^{12} cm^{-3} has been reported upon Bi^{3+} addition in $MAPbBr_3$ (REF.[81]). However, the bandgap narrowing observed in Bi-doped $MAPbI_3$, $MAPbCl_3$ and $CsPbBr_3$ (REFS[82–84]) has been called into question in subsequent studies, which attributed the colour change to broader Urbach tails related to an increase in energetic disorder[78,85–88]. Poor carrier generation efficiency has further been observed in Bi-doped $MAPbBr_3$; for example, a free carrier density n_{free} of ~8×10^{11} cm^{-3} results from a 2×10^{18} cm^{-3} Bi atomic concentration N_{dop} in the $MAPbBr_3$ structure[81]. Considering the doping efficiency defined as $\eta_{dop} = n_{free}/N_{dop}$, we deduce that only ~$10^{-5}$% of the impurities ionize and η_{dop} further decreases as the Bi concentration increases. Bi^{3+} doping has been suggested to introduce defects rather than direct carrier supply[85], supported by the significant increase in electron and hole recombination rates[87] (FIG. 3b). Formation of deep defects, as suggested by DFT calculations[39], could be consistent with poor ionization efficiency, raising doubts of the ability of Bi^{3+} to act as an efficient dopant. As a consequence of charged defect formation, which leads to scattering centres, a mobility decrease is observed with doping[87]. Nevertheless, a five orders of magnitude increase in carrier density of up to ~2×10^{16} cm^{-3} at 10 mol% Bi in solution has been reported[89], which is higher than the saturation previously observed in Bi-doped $MAPbBr_3$ (REF.[81]), evidently overcoming the limitation from intrinsic defect formation suggested by DFT for $MAPbBr_3$ (REF.[39]). Although there is consensus in terms of the detrimental effects of Bi^{3+} doping on charge transport and recombination in several Pb-based perovskites, the position of Bi^{3+} in the structure (for example, interstitial, substitutional or segregation) and the ability of Bi^{3+} to effectively generate free carriers remain to be determined.

Other substitutions also impact carrier density and E_F position in HaPs. For example, Ag_{Pb} was used as p-type dopant to compensate the n-type doping of native $MAPbI_3$ (REF.[90]) or to further p-dope $CsPbBr_3$

Table 2 | **Doping densities and Fermi level positions achieved by extrinsic defect doping**

Compound and processing	State	Type	*n* (cm^{-3})	*p* (cm^{-3})	E_C-E_F (meV)	E_F-E_V (meV)	Technique	Ref.
$MAPbI_3$								
Group I								
Rb (RbI in solution)	0 mol	n	1.0×10^{12}	–	–	–	Hall	75
	1.8 mol	p	–	5.0×10^{11}	–	–		
Na (NaI in solution)	0 mol	n	1.0×10^{12}	–	–	–	Hall	74
	0.22 mol	p	–	1.0×10^{12}	–	–		
Group IB								
Cu (CuSCN in solution)	0 mg ml^{-1}	n	–	–	140	–	UPS	77
	15 mg ml^{-1}	p	–	–	–	600		
Ag (AgI in solution)	0 mol%	n	5.1×10^{16}	–	90	–	Capacitance; UPS	90
	1 mol%	n	1.6×10^{16}	–	440	–		
Group V								
Sb ($SbCl_3$ in solution)	0 mol%	n	7.2×10^{14}	–	810	–	Hall; UPS	79
	2 mol%	n	8.3×10^{16}	–	470	–		
Sb (SbI_3 in solution)	0 mol%	n	–	–	~700	–	STS	80
	10 mol%	n	–	–	~500	–		
Group VI								
O (O_2 exposure)	Vacuum	n	–	–	200	–	From W_f using KP	72
	O_2	n	–	–	700	–		
$MAPbBr_3$								
Group V								
Bi ($BiBr_3$ in solution)	0 mol%	n	~10^9	–	–	–	Hall	81
	5 mol%	n	~10^{12}	–	–	–		
$CsPbBr_3$								
Group IB								
Ag (Ag^+ precursor) ($CsPbBr_3$ NCs)	0 mol%	p	–	–	–	1,100	UPS	91
	0.48 mol% (ICP-EOS)	p	–	–	–	600		
Group V								
Bi ($BiBr_3$ in solution) ($CsPbBr_3$ NCs)	0 mol%	p	–	–	–	340	From W_f using KP and PESA	93
	2.1 mol%	p	–	–	–	530		
$MASnI_3$								
Group IV								
Sn^{4+} (SnI_4 in solution)	0 mmol	p	–	9×10^{17}	–	–	Hall	29
	0.2 mmol	p	–	7×10^{18}	–	–		
$CsSnI_3$								
Group IV								
Sn^{4+} (air exposure)	0 min	p	–	2.4×10^{18}	–	–	Hall	100
	12 min	p	–	1.1×10^{19}	–	–		
$MA_3Sb_2I_9$								
Group IV								
Sn (SnI_4 in solution)	Sn/Sb = 0	p	–	–	–	~1,000	STS	102
	Sn/Sb = 0.5	n	–	–	~500	–		

The table displays the type (p or n), electron density *n*, hole density *p*, difference between the conduction band minimum energy E_C and the Fermi level E_F (E_C-E_F), difference between E_F and the valence band maximum energy E_V (E_F-E_V) and the technique used for the analysis for each material doped with a given concentration or processing (state). ICP-OES, inductively coupled plasma optical emission spectroscopy; KP, Kelvin probe; NCs, nanocrystals; PESA, photoelectron spectroscopy in air; STS, scanning tunnelling spectroscopy; UPS, ultraviolet photoelectron spectroscopy.

nanocrystals[91,92]. $CsPbBr_3$ nanocrystals also exhibit less p-type behaviour compared with the undoped material with Bi_{Pb} as n-type dopant[92,93]. Further comparison of bulk and nanocrystal behaviour with similar extrinsic dopants would be particularly interesting. Li^+ cations have been used as n-dopant in various perovskites; a 440-meV E_F up-shift has been measured in Li-doped $MAPbI_3$, leading to reduced non-radiative losses through trap filling[94]. $CsPbBr_3$ can be electrochemically n-doped with Li^+, resulting in improved electron injection efficiencies[95] (FIG. 3c). Moreover, Li^+ diffusion from a bis(trifluoromethane)sulfonimide lithium (Li-TFSI)-doped hole transport layer leads to unintentional doping of the perovskite active layer[96]. Indeed, Li^+ has proven to be effectively stored in perovskites through electrochemical reactions for applications in Li-ion batteries[97,98]; in addition, DFT calculations suggest energetically favourable interstitial occupancy compared with A-site substitutions[99]. Sn^{2+} oxidation (air exposure) or substitution with Sn^{4+} in the precursor solution leads to an order of magnitude increase in hole density in Sn-based HaPs[27–29,100]. Although substitution of Sn^{2+} with a higher oxidation state, such as Sn^{4+}, should lead to n-type doping, p-doping has been experimentally observed, owing to the concomitant formation of Sn vacancies (V_{Sn}), which possess a low formation energy in Sn-based perovskites[38,40,41]. Indeed, increasing V_{Sn} formation energy through partial Pb substitution of Sn leads to increased stability to oxidation[41,101]. Introducing Sn^{4+} in the 0D perovskite $MA_3Sb_2I_9$ results in a transition from weak p-type to n-type, as measured by scanning tunnelling spectroscopy[102].

In future impurity-based doping studies, several key points should be considered when conducting and interpreting experiments. It is important to establish the difference between the dopant quantity added in the growth solution and the amount effectively introduced in the film or crystal. Furthermore, the dopant location is important, including whether it segregates at surfaces or interfaces or whether it incorporates in the perovskite structure as a substitutional or interstitial atom. Additionally, care needs to be taken regarding the potential influence of the added impurity on the perovskite stoichiometry, either owing to variations in the starting solution precursor ratio or changes in the crystallization process. Further work is also required to improve extrinsic defect doping efficiency. For example, a new technique for B-site substitution uses a metal carboxylate solution to anchor the dopant elements to the perovskite surface[103]. Dopant solubility within a structure may also depend on growth conditions[104]; for example, Pb-substituting dopants may be more soluble under host Pb-poor conditions. Moreover, a well-dissolved impurity with appropriate oxidation state does not guarantee ionization; the transition energy, usually evaluated by DFT calculations, also plays a vital role in deciding the relevance of an impurity in a host. A major obstacle to carrier generation is charge compensation, for example, involving intrinsic defects[39,70]. Impurity doping can be improved by applying appropriate growth conditions that limit the formation of compensating defects[104]. Therefore, n-doping and p-doping in $MAPbI_3$ may be improved under PbI_2-rich and MAI-poor or in PbI_2-poor and MAI-rich growth conditions, respectively.

Charge transfer doping. Changes in perovskite electronic structure can arise through charge transfer between the semiconductor and a third-party entity, located either at a surface or at a grain boundary. Ultraviolet, inverse and X-ray photoelectron spectroscopy characterization can reveal the influence of the substrate on perovskite W_f and E_F (REFS[105–108]). The substrate disposition (p-type or n-type) directly impacts E_F in the $MAPbI_3$ overlayer[105] (FIG. 4a). Although different substrates may induce different defect formation energies, leading to variable E_F positions, charge transfer is the most likely cause for E_F pinning if alignment with the substrate W_f is observed. n-Type substrates, such as TiO_2 or ZrO_2, donate electrons to the perovskite, therefore, shifting E_F towards the CBM, whereas p-type substrates, such as Cu_2O, donate holes and move E_F towards the VBM. A similar substrate dependence has been observed if TiO_2 is replaced by NiO_x, which changes $MAPbI_3$ from n-type to slightly p-type[106]. These observations indicate a low density of intrinsic carriers and mid-gap states, because substrates dictate the E_F position deep into the perovskite layer. Ultraviolet photoelectron spectroscopy measurements of incrementally evaporated $MAPbI_3$ on various substrates (indium tin oxide (ITO), MoO_3, poly(3,4-ethylenedioxythiophene)-poly(styrenesulfonate) (PEDOT:PSS) and polyethylenimine ethoxylated (PEIE)) further confirm the impact of the substrate W_f on the perovskite E_F position and demonstrate the formation of interface dipoles and band bending in the perovskite layer following charge redistribution[108]. Therefore, the E_F position in low-carrier-density semiconductors, such as most perovskites, must be analysed with caution (that is, different substrates may lead to different results). In addition, MoO_3 has been used to intentionally p-dope $CsPbBr_3$ nanowires through charge transfer in a core–shell structure[109]. Substrate W_f can also be tuned through surface treatments (for example, with ionic liquids)[110,111], which impact the E_F position in the adjacent perovskite layer. For example, a perovskite grown on a SnO_2 electron transport layer, treated with fluorinated ionic liquid, exhibits a trap density lower by an order of magnitude compared with untreated SnO_2 (REF.[110]). This passivation effect or lower tendency of defect formation with treated SnO_2 is attributed to the charge-transfer-induced n-doping effect of the ionic liquid, as observed with ultraviolet photoelectron spectroscopy measurements. Nevertheless, E_F tuning with the substrate W_f is generally not appropriate to achieve high carrier densities, owing to the range of W_f available for common substrates, thereby, limiting the charge transfer processes with the perovskite.

More efficient charge transfer may be induced through deposition of appropriate molecular donors and acceptors, which n-dope or p-dope the semiconductor locally without disrupting the crystal structure[112] (FIG. 4b). Surface charge transfer doping with molecules has previously been used in organic semiconductors and inorganic materials, such as diamond, graphene or silicon[112–116], and has also been reported for perovskite materials[117–119].

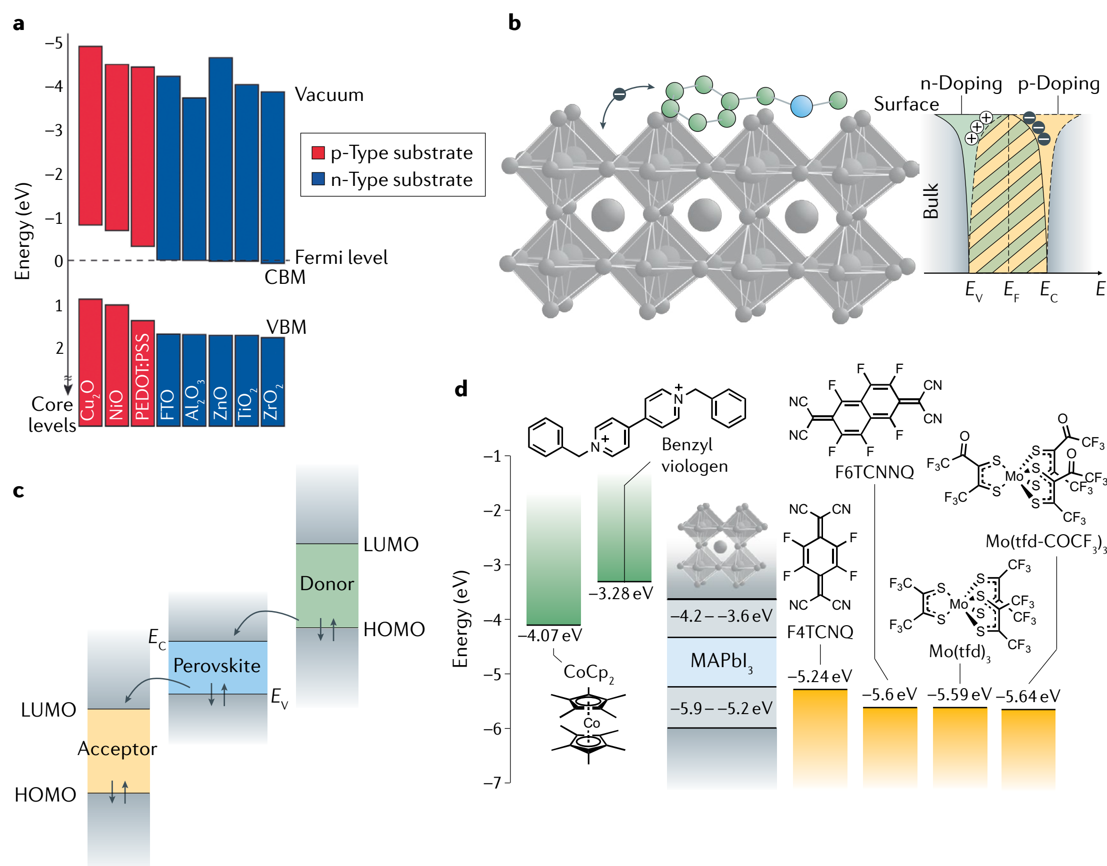

Fig. 4 | **Charge transfer doping in halide perovskites. a** | Fermi level position in $MAPbI_3$ (where MA is methylammonium) deposited on various substrates. The valence band maximum (VBM) is measured by ultraviolet photoelectron spectroscopy and the conduction band minimum (CBM) is determined by adding the transport gap (1.7 eV) to the VBM[105]. **b** | Schematic of charge transfer doping at the perovskite surface with a molecular dopant. The impact of surface doping on the band diagram is shown with a band bending at the interface. The direction of band bending depends on the nature of surface doping: n-type (solid line filled in green) and p-type (dashed line filled in orange). E is the energy with respect to the vacuum level, E_F corresponds to the Fermi energy, and E_C and E_V are the CBM and VBM energies, respectively. **c** | Schematic showing the highest occupied molecular orbital (HOMO) and lowest unoccupied molecular orbital (LUMO) relative positions expected to allow charge transfer doping from molecular donors and acceptors to the perovskite. **d** | HOMO and LUMO of common n-type and p-type molecular dopants[116,198–202]. The range of $MAPbI_3$ E_C and E_V values reported in the literature from ultraviolet photoelectron spectroscopy measurements are given for comparison[108,203,204]. $CoCp_2$, cobaltocene; F4TCNQ, 2,3,5,6-tetrafluoro-7,7,8,8-tetracyanoquinodimethane; F6TCNNQ, 1,3,4,5,7,8-hexafluoro-tetracyanonaphthoquinodimethane; $Mo(tfd)_3$, molybdenum tris(1,2-bis(trifluoromethyl) ethane-1,2-dithiolene); $Mo(tfd\text{-}COCF_3)_3$, molybdenum tris[1-(trifluoroethanoyl)-2-(trifluoromethyl)ethane-1,2-dithiolene; PEDOT:PSS, poly(3,4-ethylenedioxythiophene)-poly(styrenesulfonate). Panel **a** is reprinted with permission from REF.[105], Royal Society of Chemistry.

Strong acceptor and donor molecules are widely used to dope organic semiconductors through a charge transfer mechanism, which relies on the relative position of the host and dopant energy levels[120,121]. To enable charge transfer for perovskites, the dopant highest occupied molecular orbital (HOMO) must lie close to or above the perovskite CBM for n-type doping, whereas the dopant lowest unoccupied molecular orbital (LUMO) must lie close to or below the perovskite VBM for p-type doping (FIG. 4c). To estimate the potential doping ability of a molecule, the relative position of the perovskite (for example, $MAPbI_3$) E_C and E_V must, therefore, be considered (FIG. 4d). In addition to energy level alignment, the surface defect density must remain sufficiently low to allow free carrier generation in the semiconductor[115], which is generally true for HaPs that exhibit low surface recombination velocities[122,123]. Upon surface charge transfer, the molecular layer becomes negatively (or positively) charged for p-type (or n-type) doping, and the generated holes (or electrons) form a space charge region at the semiconductor surface[112] (FIG. 4b). Therefore, the generated carriers are subject to an electric field that attracts the free carriers close to the surface through coulombic interactions.

Molecular surface doping with cobaltocene ($CoCp_2$) and $Mo(tfd\text{-}COCF_3)_3$, which satisfy energetic alignment conditions with their perovskite host (FIG. 4d), resulted in n-doping and p-doping with a 620-meV up-shift and 670-meV down-shift of E_F, respectively[117,118]. Moreover, ionization of the Mo-based dopant and, therefore, charge transfer have been verified using nuclear magnetic resonance spectroscopy[118]. Despite localized

doping at the perovskite surface, the lateral conductivity of the 120-nm-thick $MAPbI_3$ film treated with $CoCp_2$ increases by two orders of magnitude compared with the untreated film[117], suggesting efficient generation of carriers (assuming constant mobility). Two different zethrene molecules have also been explored for surface n-doping and p-doping of $CsPbBr_3$ (REF.[119]). Furthermore, surface p-doping with the hole transport material 4,4′,4″,4‴-(pyrazine-2,3,5,6-tetrayl) tetrakis (N,N-bis(4-methoxyphenyl)aniline) (PT-TPA) has been reported[124]. However, with a LUMO at approximately −1.5 eV, charge transfer from the perovskite VBM to the dopant LUMO and, therefore, p-doping, appears unlikely. In addition, introduction of molecular dopants throughout the perovskite film thickness has been investigated. For example, the acceptor molecule 2,3,5,6-tetrafluoro-7,7,8,8-tetracyanoquinodimethane (F4TCNQ) has been introduced in the precursor solution to p-dope $MAPbI_3$, improving the efficiency of hole-transport-layer-free solar cells[125], with an order of magnitude increase in conductivity and a factor of four increase in carrier density (from capacitance) at an incorporation of 0.03 wt% F4TCNQ. F4TCNQ has further been used in $MAPbI_3$-based perovskite solar cells to suppress recombination at grain boundaries and improve the PCE[126]. 1,3-Dimethyl-2-phenyl-2,3-dihydro-1H-benzoimidazole (DMBI) derivatives have been introduced in $MAPbI_3$ films, leading to n-type doping, with an E_F shift of up to 520 meV towards the CBM, as obtained from ultraviolet photoelectron spectroscopy[127].

Molecular doping of $CsPbI_3$ nanocrystals with the p-dopant F4TCNQ and the n-dopants benzyl viologen and $CoCp_2$ has been achieved through immersion of the perovskite films in dopant-containing solutions[128]. Doping resulted in an increase in conductivity by a factor of 2.5 for F4TCNQ and a decrease of the initial p-type conductivity by a factor of 10 with benzyl viologen and $CoCp_2$, attributed to doping compensation. Ultraviolet photoelectron spectroscopy measurements show a 560-meV E_F up-shift upon n-doping with benzyl viologen, despite a lack of strong electron conductivity enhancement, expected for an E_F of 160 meV below the CBM. Additionally, questions arise regarding the possibility for charge transfer, owing to the energetic barrier of 570 meV between the $CsPbI_3$ VBM and the F4TCNQ LUMO, suggesting inefficient p-doping of the semiconductor (given a thermal energy of only ~26 meV at room temperature).

HaP molecular doping remains underexplored and further work is required to assess and better understand the interactions between the host and the dopant. Moreover, the location of the molecular dopant in the film remains uncertain; that is, whether the dopant segregates at the surface or at grain boundaries or, less likely for 3D perovskites, enters the crystal lattice. If the dopant segregates at surfaces, it is of interest whether dopant clumping occurs or whether the dopant forms a uniform coating, and how this impacts doping efficiency.

Doping characterization and assessment

Electrical doping directly impacts semiconductor carrier density. Therefore, film conductivity, σ, represents an easy and convenient first check for doping, although no firm conclusions can be drawn from this measurement because both mobility and carrier density control conductivity. The extraction of the resistance from single current–voltage (I–V) (two-point probe) measurements may further be flawed by poor contact quality[129]. Four-point-probe techniques or the transfer length method should be used to measure bulk resistivity and avoid measurement errors owing to contact resistance[129,130]. Resistivity must be extracted in the ohmic regime, where the resistance does not vary with the applied bias. Conductivity evolutions below one order of magnitude have been reported with doping[52,74–76,118,125,127,128,131,132]. Considering the often strong sample-to-sample variability in perovskites (even within a laboratory, using the same film preparation approach), which can exceed an order of magnitude (TABLE 1), statistics are crucial to verify the reproducibility of such limited evolution. Additionally, potential persistent photoconductivity phenomena may arise in HaPs[133], which can lead to erroneous conductivity and carrier density values. Indeed, measurements performed in the dark, before thermal equilibrium is reached for a light-exposed film, may lead to overestimation of the dark conductivity and variability among measurements. Ageing issues can also interfere with accurate assessment of doping. In particular, Sn-based perovskites readily oxidize, potentially promoting more pronounced p-type doping with time[60].

To confirm that conductivity increase originates from electrical doping rather than mobility variation, carrier density and/or the E_F position should be directly measured (FIG. 5). Mott–Schottky analysis using capacitance–voltage (C–V) measurements provide the ionized dopant density (N_D^+ or N_A^-), often assumed to be identical to the free carrier densities (n or p)[130]. By applying a reverse bias to a Schottky diode, a space charge region of width w forms and N_D^+ or N_A^- is obtained from the slope $d(1/C^2)/dV$. Basic Mott–Schottky analysis relies on the depletion approximation (no free carriers in the depletion region)[130], which may not always be satisfied. The validity of the Mott–Schottky analysis has been called into question in organic p-i-n solar cells[134], owing to the limited density range that can be probed, which causes overestimation of the doping concentration for intrinsic or slightly doped semiconductors. Similar limitations can be expected in p-i-n perovskite solar cells. Moreover, the requirement that the depletion region must extend across the perovskite material[130] may not be met for certain device structures, including those with organic semiconductor hole and electron transport layers. Indeed, charge transport layers have an impact on the capacitance response of perovskite solar cells and are responsible for discrepancies in reported ε_r values[135]. To properly exclude capacitive contributions from the hole and electron transport layers, Schottky devices with appropriate structures must be designed for C–V measurements. Additionally, the signal frequency must be carefully selected to avoid parasitic capacitive responses, the extraction regime in the Mott–Schottky plot properly identified and a slow sweep rate employed to avoid hysteresis issues[136]. As Mott–Schottky-derived carrier densities often substantially exceed values obtained by Hall

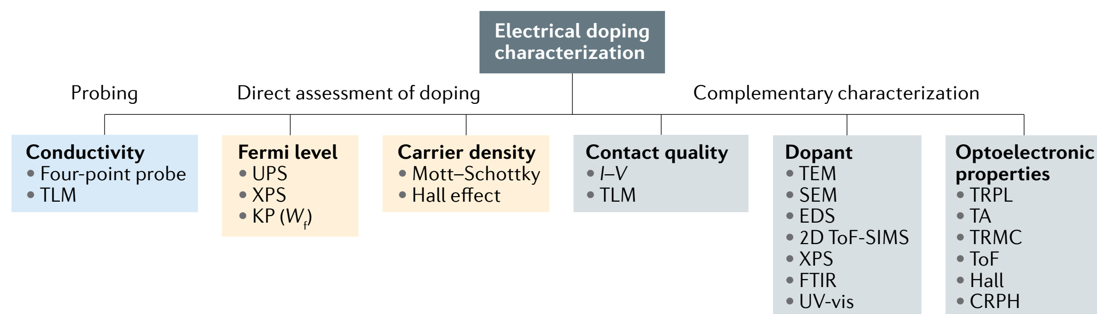

Fig. 5 | **Characterization of doping.** Conductivity measurement provides a convenient way to probe potential doping, but may be impacted by changes in mobility. Direct assessment of doping includes carrier density and Fermi level position studies, which can probe and quantify doping. Complementary characterizations include changes in Fermi level position, which also impacts contact quality and injection mechanisms. The ability to directly probe the dopant can provide information on its localization and ionization within the film or crystal. The impact of doping on various perovskite optoelectronic properties is also of interest. 2D ToF-SIMS, 2D time-of-flight secondary-ion mass spectrometry; CRPH, carrier-resolved photo-Hall; EDS, energy-dispersive X-ray spectroscopy; FTIR, Fourier-transform infrared spectroscopy; *I*–*V*, current–voltage; KP, Kelvin probe; SEM, scanning electron microscopy; TA, transient absorption; TEM, transmission electron microscopy; TLM, transfer length method; ToF, time-of-flight; TRMC, time-resolved microwave conductivity; TRPL, time-resolved photoluminescence; UPS, ultraviolet photoelectron spectroscopy; UV-vis, ultraviolet–visible absorption spectroscopy; W_f, work function; XPS, X-ray photoelectron spectroscopy.

measurements (TABLES 1,2), questions arise regarding the correct interpretation of results.

As an alternative to Mott–Schottky analysis, steady-state Hall effect measurements (BOX 1) enable the determination of carrier density and type (n-type or p-type). However, this technique requires ohmic contacts (which are not always easily achievable with perovskites) and is limited by sensitivity. Standard Hall setups with static (DC) magnetic fields are insufficient for examining low mobility ($\leq 1\,cm^2\,V^{-1}\,s^{-1}$) and high sheet resistance ($\geq 10\,M\Omega sq^{-1}$) semiconductors, such as most perovskites. To increase the signal-to-noise ratio and reduce the impact of drifting background signal, an oscillating (AC) magnetic field must be used in combination with lock-in detection[137,138]. A high-purity single harmonic and unidirectional field alleviates higher harmonic content in the Hall signal[139]. For example, a parallel dipole line system can be applied to extract Hall signals as demonstrated in $(FA,MA)Pb(I,Br)_3$ and $MAPbI_3$ (up to $40\,G\Omega sq^{-1}$)[48,137,139]. Owing to the difficulty in extracting reliable Hall signals from transverse resistance measurements, which always give a numerical value (correct or incorrect), details need to be provided for the nature of signal extraction and statistics. Moreover, the scattering factor r (which lies between 1 and 2), which is usually not known for new semiconductors and depends on the magnetic field and the temperature, needs to be assumed[130]. A typical assumption is $r=1$, which should not lead to an error of >30%. Nevertheless, r may change with doping.

Photoelectron spectroscopies, that is, ultraviolet and X-ray photoelectron spectroscopy, and Kelvin probe measurements, can be used to study the impact of doping on the electronic properties of a semiconductor surface[140,141] (BOX 2). Upon electrical doping, E_F shifts towards the CBM (or the VBM) because electrons (or holes) are added to the structure. Therefore, determining the E_F position within the bandgap allows quantification of doping (using Eqs (3) and (4)). Kelvin probes, which require calibration of the tip W_f (REF.[142]), measure the contact potential difference at the semiconductor surface, enabling the extraction of the perovskite W_f at the surface[143]. However, W_f determination is insufficient to confidently infer successful doping, because changes in W_f may also arise owing to the formation of interfacial dipoles. To confirm doping, photoelectron spectroscopy can be used to determine the E_F position relative to the VBM, which can be further corroborated by other measurements (for example, scanning tunnelling spectroscopy)[143]. However, problems can arise during measurement and analysis. For example, substrate W_f can have a strong impact on the measured E_F in nearly intrinsic perovskites. With increasing free carrier density, E_F is expected to become independent of the substrate W_f and shift closer to the VBM or the CBM. Therefore, it is important to be aware of E_F pinning effects and variable depletion width in materials with varying carrier density.

Ultraviolet and X-ray photoelectron spectroscopy use high-energy radiation to probe electrons and, thus, may degrade samples, leading to misinterpretation of data[140]; for example, illumination in vacuum leads to long-term changes in the perovskite surface W_f owing to the loss of halide species[142]. Moreover, the high-vacuum environment in photoelectron spectroscopy measurements may have an impact on the E_F position, which can shift towards the CBM, as observed for various lead HaPs[144]. VBM extraction and, thus, determination of the associated relative position to E_F, by common linear extrapolation of ultraviolet photoelectron spectroscopy data to the background level may lead to overestimation of the ionization potential, owing to low density of states near the VBM; therefore, a logarithmic detection mode and analysis have been suggested to be more appropriate for HaPs[142]. In addition, photon line satellites must be subtracted because they can be mistakenly attributed to gap states extending above the VBM[142]. X-ray photoelectron spectroscopy can also provide information on doping, based on the expected rigid shift of the core level

Box 1 | **Hall effect measurements**

Hall effect measurement relies on the Lorentz force experienced by free carriers when exposed to a magnetic field[34]. A magnetic field $\vec{B}$ applied perpendicular to the semiconductor layer and to the current (I) direction deflects carriers towards one side of the Hall bar, owing to the magnetic force $q\vec{v} \times \vec{B}$, where $\vec{v}$ corresponds to the carrier velocity and q to the electric charge (q = −e for electrons and q = +e for holes).

The created transverse voltage is called the Hall voltage V_H, and a Hall coefficient H can be extracted from the relation $H = dV_H/IB$, with d representing the sample thickness. The carrier density n_{Hall} can be deduced from H according to the relation $H = r/qn_{Hall}$, with the scattering factor r lying between 1 and 2, depending on the scattering mechanism in the semiconductor[130]. Therefore, the sign of the Hall coefficient reveals the semiconductor type (n or p) and the associated value provides the majority carrier density. The sample conductivity σ can be determined by measuring the longitudinal voltage with a four-point-probe technique, and, thus, the majority carrier mobility can be calculated using $\mu_{n/p} = \mp\sigma H$. The measurement must be performed in the dark for these equations to be valid. Under illumination, electrons and holes need to be taken into account, leading to more complex formulae[130].

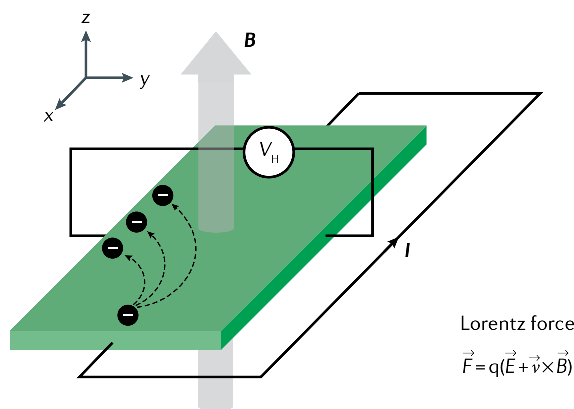

positions. n-Type or p-type doping leads to a E_F shift towards the CBM (or the VBM), increasing (or decreasing) the binding energy E_B. However, charging effects can also cause an apparent E_B shift, thereby, leading to wrong conclusions[140]. Furthermore, photoelectron spectroscopy and Kelvin probe characterization techniques probe the sample surface, which may have a different electronic structure than the bulk. Surface contaminants and defects also have an impact on measurements, and surface cleaning, for example, gentle sputtering or heating, likely impacts HaP surface chemistry. Despite these caveats, direct measurement of E_F shift provides an important pathway to validate and quantify intrinsic and extrinsic doping in perovskites (TABLES 1,2).

Doping also has an impact on the injection current at a Schottky contact. Heavy doping of the semiconductor can transform a Schottky contact to an ohmic contact by reducing the depletion width at the interface, enabling carrier tunnelling (FIG. 1d) and enhancing injection and collection of charges[33]. I–V measurements on single-carrier Schottky diodes with undoped and doped perovskites and analysis of underlying mechanisms (that is, thermionic emission, tunnelling and space-charge-limited current) should provide evidence of doping and information on injection and transport properties[145,146]. Although such characterization has not yet been widely applied for HaPs[95] (FIG. 3c), it is commonly used to assess electrical doping in organic semiconductors[145–148], and could also be applied to analyse doping for contact quality improvement, enabling hole and electron transport layer-free perovskite devices.

To confirm doping potential, the impact on the dopant itself can be assessed. For charge transfer doping with molecules, optical spectroscopy can be applied to detect dopant ionization at high dopant concentrations (typically >5–10 mol%). For example, the F4TCNQ anion leads to the formation of absorption peaks at ~1.4–1.7 eV, which are visible if dopant ionization occurs in the semiconductor host (and if host absorption does not prevail in this energy range)[149]. Additionally, the cyano-vibrational bands of F4TCNQ shift to lower wavenumber upon ionization and can be measured by Fourier-transform infrared spectroscopy[150]. The doping efficiency in F4TCNQ-doped organic semiconductors is often assessed by the degree of charge transfer extracted from Fourier-transform infrared spectroscopy measurements[149]. Similar measurements could be performed in F4TCNQ-doped perovskites and extended to other molecular dopants. X-ray photoelectron spectroscopy can further probe the oxidation state of an introduced impurity (for example, extrinsic dopant)[150]. X-ray diffraction can detect secondary phases, such as excess PbI_2 (REFS[47,48]), but, often, cannot detect changes in the crystal structure at the low-impurity concentrations typically used for electrical doping[76,81,90].

The ability to detect the molecular dopant or impurity is necessary to determine its localization in the perovskite layer (for example, at the surface, grain boundaries or within the bulk crystalline lattice) and to assess the potential formation of aggregates or clusters. Transmission electron microscopy, scanning electron microscopy (SEM) and energy-dispersive X-ray spectroscopy (EDS) can be used to localize the dopant. SEM requires a strong difference in average atomic number for backscattered electron mode SEM analysis and EDS requires a sufficiently high dopant concentration for elemental analysis[151]. For example, excess PbI_2 or SnF_2 phases have been observed in SEM and transmission electron microscopy images of perovskites, confirmed by EDS analysis[48,67,152]. Large molecular dopants can be probed by SEM, if they form aggregates, as demonstrated in organic semiconductors[153]. Alternative imaging spectroscopy techniques can also be considered, for example, 2D time-of-flight secondary-ion mass spectrometry or near-field optical microscopy (for example, in the infrared range to probe molecular dopants) to map dopant-rich regions with a resolution of 20–100 nm (REFS[96,154,155]). Time-of-flight secondary-ion mass spectrometry can further probe dopant distribution as a function of depth for the perovskite layer. For paramagnetic impurities, nuclear magnetic resonance spectroscopy has been suggested to confirm substitutional doping and to allow assessment of cluster formation[156].

In addition to confirming doping and dopant distribution, the impact of the dopant on optoelectronic properties beyond carrier density can be analysed. The evolution of mobility and carrier lifetime reflects changes in scattering and recombination mechanisms, as well as trap-filling phenomena[63,157]. A variety of characterization techniques can be used to extract optoelectronic parameters, including time-resolved photoluminescence, transient absorption spectroscopy, THz spectroscopy, time-of-flight time-resolved microwave conductivity,

Hall effect and carrier-resolved photo-Hall[137,158,159]. Nevertheless, limitations of each technique and analysis need to be considered to prevent dissemination of misleading results. Importantly, most of the tools commonly used for doping analysis are advanced characterization techniques, which require expertise to analyse experimentally obtained numerical values[160,161]. It is also important to report the experimental setup and conditions to ensure reproducibility, confirm findings with different characterization techniques and critically assess experimental evidence.

Outlook

Controllable doping in HaPs is a critical step for optoelectronic device optimization. For example, the ability to dope perovskites at interfaces could improve metal–perovskite interfaces, with the aim of removing additional electron and hole transport layers, therefore, reducing device production costs[162]. A good contact facilitates carrier injection and extraction, providing low-contact resistance and avoiding significant voltage drops at the interfaces (for example, for solar cells, light-emitting diodes or transistors). Nevertheless, a quasi-ohmic contact created upon doping requires high local dopant densities with limited diffusion into the undoped perovskite region, which remains to be demonstrated for HaPs. Moreover, direct contact of the perovskite surface with the electrode requires inert conducting materials to avoid chemical reaction with the semiconductor layer, which is not an easy task for HaPs[163–165]. The ability to relax stringent requirements of the electrode W_f (by doping) should facilitate the development of adequate contact materials.

HaP p–n junctions may also be developed, assuming the possibility to strongly dope perovskites without dopant migration. Indeed, p–n junctions have been reported in perovskite solar cells[49,53]; however, the stability and efficacy of these structures remain uncertain[166,167]. For example, Cui et al.[53] use a precursor ratio variation to modulate $MAPbI_3$ carrier densities between $p=8\times10^9\,cm^{-3}$ and $n=4\times10^{12}\,cm^{-3}$ and form a p–n junction, which improves solar cell efficiency compared with a reference p-i-n structure. However, facile ionic mobility remains a problem for perovskite doping and device design[168,169], because it promotes defect inter-diffusion between initially p-doped and n-doped layers. Thus, the improved performance suggested by Cui et al.[53] may actually be a result of improved optoelectronic properties owing to slight n-doping throughout the perovskite layer following defect inter-diffusion[166]. In addition, the formation of an effective p–n homojunction is unlikely with such low doping densities; indeed, doping concentrations N_D and N_A beyond $10^{16}\,cm^{-3}$ are required to ensure a sufficiently small depletion width with respect to the perovskite thickness[167].

In addition to carrier density and E_F tuning, semiconductor optoelectronic properties, such as mobility or carrier recombination lifetime, also depend on doping. For example, doping may have a negative impact on the mobility μ_{eff}, owing to a reduction of $\mu_{impurity}$ with increasing density of coulombic scattering centres, which may become the limiting factor for mobility at room temperature (Eq. (6))[170,171]. Polar optical phonons have been identified as major scattering mechanisms in 3D perovskites[172–174]; however, trap-filling phenomena upon irradiation of the perovskite have also been reported[94,175–178], suggesting that μ_{defect} could also be a limiting factor. Low-level electrical doping could perform such trap passivation, thereby, improving μ_{defect} and μ_{eff}. Improvement of charge transport properties through trap filling with dopants has been achieved in organic semiconductors[157,179–184], which exhibit strong structural and energetic disorder. Therefore, mobility and carrier density evolutions need to be decoupled in conductivity measurements to understand doping. The introduction of free carriers also impacts the monomolecular recombination rate k_1 (Eq. (7)), which is orders of magnitude higher in $MASnI_3$ than in $MAPbI_3$, owing to self-doping of Sn (REF.[35]). An increase in k_1 implies a decrease in carrier recombination lifetime τ and diffusion length L_D; for example, in $FASnI_3$, an increase in radiative recombination between photogenerated minority carriers and background majority carriers from self-doping has been suggested[185]. Therefore, a thorough understanding of doping involves the study of its impact on semiconductor optoelectronic properties.

Despite substantial progress, the doping efficiency achieved in HaPs remains limited and the key question remains: can we dope HaPs and to what extent? Compensation represents a key issue, because it is influenced by the E_F position within the bandgap[39,44,70]

Box 2 | Electronic levels and photoelectron spectroscopy

The semiconductor energy levels are defined with respect to the vacuum level E_{vac}, the energy of an electron at rest just outside the surface of the solid[143]. The Fermi level E_F, which is located in the bandgap for a non-degenerate semiconductor, is defined at 50% probability of electron occupancy following the Fermi–Dirac distribution. Therefore, the work function W_f is defined as $W_f=E_{vac}-E_F$. Although E_{vac} is highly dependent on the nature of the semiconductor surface, including the formation of dipoles, E_F depends on the density of states, carrier density, doping concentration and temperature[143]. The electron affinity (EA) and ionization potential (IP), both positive values, correspond to the energy difference between E_{vac} and the conduction band minimum (CBM) and valence band maximum (VBM), respectively. The bandgap energy E_G is the energy difference between VBM and CBM energies.

Photoelectron spectroscopy, such as ultraviolet photoelectron spectroscopy and X-ray photoelectron spectroscopy, rely on the photoelectric effect to excite electrons upon irradiation with high-energy photons $h\nu$[140]. The kinetic energy E_{kin} is measured and the photoelectron binding energy E_B is extracted using the relation:

$$E_{kin}=h\nu-E_B-W_f,$$

where W_f is the spectrometer work function. Ultraviolet photoelectron spectroscopy probes electrons in the valence band and helps identify the VBM and its position relative to the Fermi level, whereas X-ray photoelectron spectroscopy probes core level electrons to study the chemical properties of the surface. X-ray photoelectron spectroscopy may also provide information about the position of E_F with respect to the VBM.

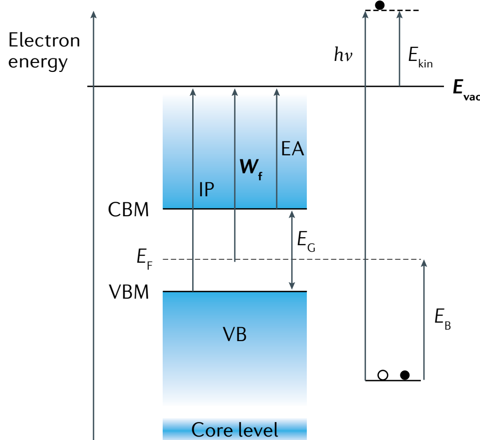

and observed in various materials (for example, wide-bandgap semiconductors)[104,186,187]. Compensation prevents strong ambipolar p-type and n-type doping for most HaPs. Limitations resulting from self-compensation may possibly be overcome by using non-equilibrium growth conditions[188]. For example, DFT calculations have shown that, for CdTe (a similar bandgap semiconductor as the most commonly explored HaPs for perovskite applications), processing under high-temperature growth conditions, which enhances defect formation, followed by rapid quenching to avoid self-compensation, allows tuning of E_F beyond the thermodynamic limit[189]. Nevertheless, non-equilibrium growth approaches remain to be tested in HaPs and face experimental challenges, such as HaP decomposition at elevated temperatures. Compensation might not be the only challenge for doping efficiency in HaPs. The validity of the commonly used static point defect model (generally assumed in DFT calculations) has been questioned and predominance of dynamic defects (~ps lifetime) highlighted[190,191]. Dynamic disorder leads to the desired self-healing ability of perovskites, but complicates traditional doping, which requires kinetically stabilized defects to prevent the re-formation of the lattice. To circumvent problems dictated by the dynamic nature of defects, doping by charge transfer at surfaces and grain boundaries may be a promising solution. In particular, perovskite nanocrystals have a high surface-to-volume ratio for charge transfer doping. Moreover, nanocrystals provide tunable CBM and VBM levels with quantum confinement, and allow tuning of defect formation energies[128]. Bulky molecules could also be used for doping by charge transfer within grain boundaries, providing an interesting route to inhibit ion migration. Molecular dopants could further be directly introduced into the layered 2D perovskite structure to generate charge transfer between the organic and inorganic layers[192,193].

Overall, while electrical doping is key to the development of microelectronic technologies, HaP doping has proven particularly challenging. Tackling these challenges will require innovative materials design, judicious application of DFT and materials modelling, and careful and well-validated experimental characterization. Through such studies, the spatial and temporal control over charge carrier concentration in HaPs will continue to advance the development of this exceptional semiconductor class.

Published online 23 March 2021

1. Gao, P., Bin Mohd Yusoff, A. R. & Nazeeruddin, M. K. Dimensionality engineering of hybrid halide perovskite light absorbers. *Nat. Commun.* **9**, 5028 (2018).
2. Saparov, B. & Mitzi, D. B. Organic–inorganic perovskites: structural versatility for functional materials design. *Chem. Rev.* **116**, 4558–4596 (2016).
3. Jena, A. K., Kulkarni, A. & Miyasaka, T. Halide perovskite photovoltaics: background, status, and future prospects. *Chem. Rev.* **119**, 3036–3103 (2019).
4. Snaith, H. J. Present status and future prospects of perovskite photovoltaics. *Nat. Mater.* **17**, 372–376 (2018).
5. Nasti, G. & Abate, A. Tin halide perovskite ($ASnX_3$) solar cells: A comprehensive guide toward the highest power conversion efficiency. *Adv. Energy Mater.* **10**, 1902467 (2020).
6. Xie, C., Liu, C., Loi, H. & Yan, F. Perovskite-based phototransistors and hybrid photodetectors. *Adv. Funct. Mater.* **30**, 1903907 (2020).
7. Wangyang, P. et al. Recent advances in halide perovskite photodetectors based on different dimensional materials. *Adv. Opt. Mater.* **6**, 1701302 (2018).
8. Yang, T. et al. Understanding, optimizing, and utilizing nonideal transistors based on organic or organic hybrid semiconductors. *Adv. Funct. Mater.* **30**, 1903889 (2020).
9. Liu, X., Yu, D., Song, X. & Zeng, H. Metal halide perovskites: Synthesis, ion migration, and application in field-effect transistors. *Small* **14**, 1801460 (2018).
10. Quan, L. N. et al. Perovskites for next-generation optical sources. *Chem. Rev.* **119**, 7444–7477 (2019).
11. Lu, M. et al. Metal halide perovskite light-emitting devices: Promising technology for next-generation displays. *Adv. Funct. Mater.* **29**, 1902008 (2019).
12. Stylianakis, M. M., Maksudov, T., Panagiotopoulos, A., Kakavelakis, G. & Petridis, K. Inorganic and hybrid perovskite based laser devices: a review. *Materials* **12**, 859 (2019).
13. Mi, Y., Zhong, Y., Zhang, Q. & Liu, X. Continuous-wave pumped perovskite lasers. *Adv. Opt. Mater.* **7**, 1900544 (2019).
14. Haque, M. A., Kee, S., Villalva, D. R., Ong, W. L. & Baran, D. Halide perovskites: Thermal transport and prospects for thermoelectricity. *Adv. Sci.* **7**, 1903389 (2020).
15. National Renewable Energy Laboratory (NREL). Best Research-Cell Efficiency Chart. *NREL* https://www.nrel.gov/pv/cell-efficiency.html (2020).
16. Shi, B., Duan, L., Zhao, Y., Luo, J. & Zhang, X. Semitransparent perovskite solar cells: from materials and devices to applications. *Adv. Mater.* **32**, 1806474 (2020).
17. Li, Z. et al. Scalable fabrication of perovskite solar cells. *Nat. Rev. Mater.* **3**, 18017 (2018).
18. Park, N. G. & Zhu, K. Scalable fabrication and coating methods for perovskite solar cells and solar modules. *Nat. Rev. Mater.* **5**, 333–350 (2020).
19. Egger, D. A. et al. What remains unexplained about the properties of halide perovskites? *Adv. Mater.* **30**, 1800691 (2018).
20. Brenner, T. M., Egger, D. A., Kronik, L., Hodes, G. & Cahen, D. Hybrid organic–norganic perovskites: Low-cost semiconductors with intriguing charge-transport properties. *Nat. Rev. Mater.* **1**, 15007 (2016).
21. Queisser, H. J. & Haller, E. E. Defects in semiconductors: Some fatal, some vital. *Science* **281**, 945–950 (1998).
22. Zhang, X., Li, L., Sun, Z. & Luo, J. Rational chemical doping of metal halide perovskites. *Chem. Soc. Rev.* **48**, 517–539 (2019).
23. Zhou, Y., Chen, J., Bakr, O. M. & Sun, H.-T. Metal-doped lead halide perovskites: synthesis, properties, and optoelectronic applications. *Chem. Mater.* **30**, 6589–6613 (2018).
24. Goyal, A. et al. On the dopability of semiconductors and governing materials properties. *Chem. Mater.* **32**, 4467–4480 (2020).
25. Mitzi, D. B., Feild, C. A., Schlesinger, Z. & Laibowitz, R. B. Transport, optical, and magnetic properties of the conducting halide perovskite $CH_3NH_3SnI_3$. *J. Solid State Chem.* **114**, 159–163 (1995).
26. Mitzi, D. B., Feild, C. A., Harrison, W. T. A. & Guloy, A. M. Conducting tin halides with a layered organic-based perovskite structure. *Nature* **369**, 467–469 (1994).
27. Takahashi, Y. et al. Tunable charge transport in soluble organic–inorganic hybrid semiconductors. *Chem. Mater.* **19**, 6312–6316 (2007).
28. Takahashi, Y. et al. Charge-transport in tin-iodide perovskite $CH_3NH_3SnI_3$: origin of high conductivity. *Dalton Trans.* **40**, 5563–5568 (2011).
29. Takahashi, Y., Hasegawa, H., Takahashi, Y. & Inabe, T. Hall mobility in tin iodide perovskite $CH_3NH_3SnI_3$: Evidence for a doped semiconductor. *J. Solid State Chem.* **205**, 39–43 (2013).
30. Haque, M. A. Tuning the thermoelectric performance of hybrid tin perovskites by air treatment. *Adv. Energy Sustain. Res.* **1**, 2000033 (2020).
31. Sze, S. M. & Ng, K. K. *Physics of Semiconductor Devices* (Wiley, 2006).
32. McCluskey, M. D. & Haller, E. E. *Dopants and Defects in Semiconductors* (CRC, 2018).
33. Streetman, B. G. & Banerjee, S. *Solid State Electronic Devices* 5th edn (2000).
34. Kasap, S. & Capper, P. *Springer Handbook of Electronic and Photonic Materials* (Springer, 2017).
35. Johnston, M. B. & Herz, L. M. Hybrid perovskites for photovoltaics: charge-carrier recombination, diffusion, and radiative efficiencies. *Acc. Chem. Res.* **49**, 146–154 (2016).
36. Manser, J. S., Christians, J. A. & Kamat, P. V. Intriguing optoelectronic properties of metal halide perovskites. *Chem. Rev.* **116**, 12956–13008 (2016).
37. Yin, W. J., Shi, T. & Yan, Y. Unusual defect physics in $CH_3NH_3PbI_3$ perovskite solar cell absorber. *Appl. Phys. Lett.* **104**, 063903 (2014).
38. Xu, P., Chen, S., Xiang, H. J., Gong, X. G. & Wei, S. H. Influence of defects and synthesis conditions on the photovoltaic performance of perovskite semiconductor $CsSnI_3$. *Chem. Mater.* **26**, 6068–6072 (2014).
39. Shi, T., Yin, W. J., Hong, F., Zhu, K. & Yan, Y. Unipolar self-doping behavior in perovskite $CH_3NH_3PbBr_3$. *Appl. Phys. Lett.* **106**, 103902 (2015).
40. Shi, T. et al. Effects of organic cations on the defect physics of tin halide perovskites. *J. Mater. Chem. A* **5**, 15124–15129 (2017).
41. Meggiolaro, D., Ricciarelli, D., Alasmari, A. A., Alasmary, F. A. S. & De Angelis, F. Tin versus lead redox chemistry modulates charge trapping and self doping in tin/lead-iodide perovskites. *J. Phys. Chem. Lett.* **11**, 3546–3556 (2020).
42. Kim, J., Lee, S. H., Lee, J. H. & Hong, K. H. The role of intrinsic defects in methylammonium lead iodide perovskite. *J. Phys. Chem. Lett.* **5**, 1312–1317 (2014).
43. Liu, N. & Yam, C. Y. First-principles study of intrinsic defects in formamidinium lead triiodide perovskite solar cell absorbers. *Phys. Chem. Chem. Phys.* **20**, 6800–6804 (2018).
44. Yang, J. H., Yin, W. J., Park, J. S. & Wei, S. H. Self-regulation of charged defect compensation and formation energy pinning in semiconductors. *Sci. Rep.* **5**, 16977 (2015).
45. Freysoldt, C. et al. First-principles calculations for point defects in solids. *Rev. Mod. Phys.* **86**, 253–305 (2014).
46. Wang, Q. et al. Qualifying composition dependent *p* and *n* self-doping in $CH_3NH_3PbI_3$. *Appl. Phys. Lett.* **105**, 163508 (2014).
47. Paul, G., Chatterjee, S., Bhunia, H. & Pal, A. J. Self-doping in hybrid halide perovskites via precursor stoichiometry: to probe type of conductivity through scanning tunneling spectroscopy. *J. Phys. Chem. C* **122**, 20194–20199 (2018).
48. Euvrard, J., Gunawan, O. & Mitzi, D. B. Impact of PbI_2 passivation and grain size engineering in $CH_3NH_3PbI_3$ solar absorbers as revealed by carrier-resolved photo-Hall technique. *Adv. Energy Mater.* **9**, 1902706 (2019).

49. Dänekamp, B. et al. Perovskite–perovskite homojunctions via compositional doping. *J. Phys. Chem. Lett.* **9**, 2770–2775 (2018).
50. Bi, C. et al. Understanding the formation and evolution of interdiffusion grown organolead halide perovskite thin films by thermal annealing. *J. Mater. Chem. A* **2**, 18508–18514 (2014).
51. Song, D. et al. Managing carrier lifetime and doping property of lead halide perovskite by postannealing processes for highly efficient perovskite solar cells. *J. Phys. Chem. C* **119**, 22812–22819 (2015).
52. Zohar, A. et al. What Is the mechanism of $MAPbI_3$ p-doping by I_2? Insights from optoelectronic properties. *ACS Energy Lett.* **2**, 2408–2414 (2017).
53. Cui, P. et al. Planar p–n homojunction perovskite solar cells with efficiency exceeding 21.3%. *Nat. Energy* **4**, 150–159 (2019).
54. Yan, K. et al. Near-infrared photoresponse of one-sided abrupt $MAPbI_3/TiO_2$ heterojunction through a tunneling process. *Adv. Funct. Mater.* **26**, 8545–8554 (2016).
55. Levine, I. et al. Mobility-lifetime products in $MAPbI_3$ films. *J. Phys. Chem. Lett.* **7**, 5219–5226 (2016).
56. Su, Z., Chen, Y., Li, X., Wang, S. & Xiao, Y. The modulation of opto-electronic properties of $CH_3NH_3PbBr_3$ crystal. *J. Mater. Sci. Mater. Electron.* **28**, 11053–11058 (2017).
57. Xiao, Z. et al. Giant switchable photovoltaic effect in organometal trihalide perovskite devices. *Nat. Mater.* **14**, 193–197 (2015).
58. Frolova, L. A., Dremova, N. N. & Troshin, P. A. The chemical origin of the p-type and n-type doping effects in the hybrid methylammonium–lead iodide ($MAPbI_3$) perovskite solar cells. *Chem. Commun.* **51**, 14917–14920 (2015).
59. Noel, N. K. et al. Lead-free organic–inorganic tin halide perovskites for photovoltaic applications. *Energy Environ. Sci.* **7**, 3061–3068 (2014).
60. Konstantakou, M. & Stergiopoulos, T. A critical review on tin halide perovskite solar cells. *J. Mater. Chem. A* **5**, 11518–11549 (2017).
61. Chung, I. et al. $CsSnI_3$: Semiconductor or metal? High electrical conductivity and strong near-infrared photoluminescence from a single material. High hole mobility and phase-transitions. *J. Am. Chem. Soc.* **134**, 8579–8587 (2012).
62. Mitzi, D. B. & Liang, K. Synthesis, resistivity, and thermal properties of the cubic perovskite $NH_2CH{=}NH_2SnI_3$ and related systems. *J. Solid State Chem.* **134**, 376–381 (1997).
63. Milot, R. L. et al. The effects of doping density and temperature on the optoelectronic properties of formamidinium tin triiodide thin films. *Adv. Mater.* **30**, 1804506 (2018).
64. Gupta, S., Bendikov, T., Hodes, G. & Cahen, D. CsSnBr3, a lead-free halide perovskite for long-term solar cell application: Insights on SnF_2 addition. *ACS Energy Lett.* **1**, 1028–1033 (2016).
65. Gupta, S., Cahen, D. & Hodes, G. How SnF_2 impacts the material properties of lead-free tin perovskites. *J. Phys. Chem. C* **122**, 13926–13936 (2018).
66. Kumar, M. H. et al. Lead-free halide perovskite solar cells with high photocurrents realized through vacancy modulation. *Adv. Mater.* **26**, 7122–7127 (2014).
67. Liao, W. et al. Lead-free inverted planar formamidinium tin triiodide perovskite solar cells achieving power conversion efficiencies up to 6.22%. *Adv. Mater.* **28**, 9333–9340 (2016).
68. Xing, G. et al. Solution-processed tin-based perovskite for near-infrared lasing. *Adv. Mater.* **28**, 8191–8196 (2016).
69. Savill, K. J. et al. Impact of tin fluoride additive on the properties of mixed tin-lead iodide perovskite semiconductors. *Adv. Funct. Mater.* **30**, 2005594 (2020).
70. Shi, T., Yin, W.-J. & Yan, Y. Predictions for p-type $CH_3NH_3PbI_3$ perovskites. *J. Phys. Chem. C* **118**, 25350–25354 (2014).
71. Chen, Y. et al. Tuning the electronic structures of all-inorganic lead halide perovskite $CsPbI_3$ via heterovalent doping: A first-principles investigation. *Chem. Phys. Lett.* **722**, 90–95 (2019).
72. Zohar, A. et al. Impedance spectroscopic indication for solid state electrochemical reaction in $(CH_3NH_3)PbI_3$ films. *J. Phys. Chem. Lett.* **7**, 191–197 (2016).
73. Senocrate, A. et al. Interaction of oxygen with halide perovskites. *J. Mater. Chem. A* **6**, 10847–10855 (2018).
74. Yang, Y. et al. Effect of doping of NaI monovalent cation halide on the structural, morphological, optical and optoelectronic properties of $MAPbI_3$ perovskite. *J. Mater. Sci. Mater. Electron.* **29**, 205–210 (2018).
75. Bai, X. et al. Effect of Rb doping on modulating grain shape and semiconductor properties of $MAPbI_3$ perovskite layer. *Mater. Lett.* **211**, 328–330 (2018).
76. Abdi-Jalebi, M. et al. Impact of monovalent cation halide additives on the structural and optoelectronic properties of $CH_3NH_3PbI_3$ perovskite. *Adv. Energy Mater.* **6**, 1502472 (2016).
77. Liu, Z. et al. A Cu-doping strategy to enhance photoelectric performance of self-powered hole-conductor-free perovskite photodetector for optical communication applications. *Adv. Mater. Technol.* **5**, 2000260 (2020).
78. Mosconi, E., Merabet, B., Meggiolaro, D., Zaoui, A. & De Angelis, F. First-principles modeling of bismuth doping in the $MAPbI_3$ perovskite. *J. Phys. Chem. C* **122**, 14107–14112 (2018).
79. Huang, L. et al. Schottky/p-n cascade heterojunction constructed by intentional n-type doping perovskite toward efficient electron layer-free perovskite solar cells. *Sol. RRL* **3**, 1800274 (2019).
80. Chatterjee, S., Dasgupta, U. & Pal, A. J. Sequentially deposited antimony-doped $CH_3NH_3PbI_3$ films in inverted planar heterojunction solar cells with a high open-circuit voltage. *J. Phys. Chem. C* **121**, 20177–20187 (2017).
81. Abdelhady, A. L. et al. Heterovalent dopant incorporation for bandgap and type engineering of perovskite crystals. *J. Phys. Chem. Lett.* **7**, 295–301 (2016).
82. Wang, R. et al. Bi^{3+}-doped $CH_3NH_3PbI_3$: Red-shifting absorption edge and longer charge carrier lifetime. *J. Alloys Compd.* **695**, 555–560 (2017).
83. Zhang, Z. et al. Bandgap narrowing in Bi-doped $CH_3NH_3PbCl_3$ perovskite single crystals and thin films. *J. Phys. Chem. C* **121**, 17436–17441 (2017).
84. Miao, X. et al. Air-stable $CsPb_{1-x}Bi_xBr_3$($0 \le x \ll 1$) perovskite crystals: Optoelectronic and photostriction properties. *J. Mater. Chem. C* **5**, 4931–4939 (2017).
85. Yamada, Y., Hoyano, M., Akashi, R., Oto, K. & Kanemitsu, Y. Impact of chemical doping on optical responses in bismuth-doped $CH_3NH_3PbBr_3$ single crystals: Carrier lifetime and photon recycling. *J. Phys. Chem. Lett.* **8**, 5798–5803 (2017).
86. Nayak, P. et al. The impact of Bi^{3+} heterovalent doping in organic–inorganic metal halide perovskite crystals. *J. Am. Chem. Soc.* **140**, 574–577 (2018).
87. Ulatowski, A. M. et al. Charge-carrier trapping dynamics in bismuth-doped thin films of $MAPbBr_3$ perovskite. *J. Phys. Chem. Lett.* **11**, 3681–3688 (2020).
88. Lozhkina, O. A. et al. Invalidity of band-gap engineering concept for Bi^{3+} heterovalent doping in $CsPbBr_3$ halide perovskite. *J. Phys. Chem. Lett.* **9**, 5408–5411 (2018).
89. Meng, R. et al. Understanding the impact of bismuth heterovalent doping on the structural and photophysical properties of $CH_3NH_3PbBr_3$ halide perovskite crystals with near-IR photoluminescence. *Chem. Eur. J.* **25**, 5480–5488 (2019).
90. Chen, Q. et al. Ag-incorporated organic–inorganic perovskite films and planar heterojunction solar cells. *Nano Lett.* **17**, 3231–3237 (2017).
91. Zhou, S. et al. Ag-doped halide perovskite nanocrystals for tunable band structure and efficient charge transport. *ACS Energy Lett.* **4**, 534–541 (2019).
92. Zhou, S. et al. Understanding charge transport in all-inorganic halide perovskite nanocrystal thin-film field effect transistors. *ACS Energy Lett.* **5**, 2614–2623 (2020).
93. Begum, R. et al. Engineering interfacial charge transfer in $CsPbBr_3$ perovskite nanocrystals by heterovalent doping. *J. Am. Chem. Soc.* **139**, 731–737 (2017).
94. Fang, Z., He, H., Gan, L., Li, J. & Ye, Z. Understanding the role of lithium doping in reducing nonradiative loss in lead halide perovskites. *Adv. Sci.* **5**, 1800736 (2018).
95. Jiang, Q. et al. Electrochemical doping of halide perovskites with ion intercalation. *ACS Nano* **11**, 1073–1079 (2017).
96. Xiao, C. et al. Inhomogeneous doping of perovskite materials by dopants from hole-transport layer. *Matter* **2**, 261–272 (2020).
97. Vicente, N. & Garcia-Belmonte, G. Methylammonium lead bromide perovskite battery anodes reversibly host high Li-ion concentrations. *J. Phys. Chem. Lett.* **8**, 1371–1374 (2017).
98. Xia, H. R., Sun, W. T. & Peng, L. M. Hydrothermal synthesis of organometal halide perovskites for Li-ion batteries. *Chem. Commun.* **51**, 13787–13790 (2015).
99. Cao, J., Tao, S. X., Bobbert, P. A., Wong, C. P. & Zhao, N. Interstitial occupancy by extrinsic alkali cations in perovskites and its impact on ion migration. *Adv. Mater.* **30**, 1707350 (2018).
100. Liu, T. et al. Enhanced control of self-doping in halide perovskites for improved thermoelectric performance. *Nat. Commun.* **10**, 5750 (2019).
101. Leijtens, T., Prasanna, R., Gold-Parker, A., Toney, M. F. & McGehee, M. D. Mechanism of tin oxidation and stabilization by lead substitution in tin halide perovskites. *ACS Energy Lett.* **2**, 2159–2165 (2017).
102. Chatterjee, S. & Pal, A. J. Tin(IV) substitution in $(CH_3NH_3)_3Sb_2I_9$: Toward low-band-gap defect-ordered hybrid perovskite solar cells. *ACS Appl. Mater. Interfaces* **10**, 35194–35205 (2018).
103. Yang, Z. et al. Anchored ligands facilitate efficient B-site doping in metal halide perovskites. *J. Am. Chem. Soc.* **141**, 8296–8305 (2019).
104. Zunger, A. Practical doping principles. *Appl. Phys. Lett.* **83**, 57–59 (2003).
105. Miller, E. M. et al. Substrate-controlled band positions in $CH_3NH_3PbI_3$ perovskite films. *Phys. Chem. Chem. Phys.* **16**, 22122–22130 (2014).
106. Schulz, P. et al. Electronic level alignment in inverted organometal perovskite solar cells. *Adv. Mater. Interfaces* **2**, 1400532 (2015).
107. Wang, C. et al. Surface analytical investigation on organometal triiodide perovskite. *J. Vac. Sci. Technol. B Nanotechnol. Microelectron. Mater. Process. Meas. Phenom.* **33**, 032401 (2015).
108. Olthof, S. & Meerholz, K. Substrate-dependent electronic structure and film formation of $MAPbI_3$ perovskites. *Sci. Rep.* **7**, 40267 (2017).
109. Meng, Y. et al. Perovskite core–shell nanowire transistors: Interfacial transfer doping and surface passivation. *ACS Nano* **14**, 12749–12760 (2020).
110. Noel, N. K. et al. Elucidating the role of a tetrafluoroborate-based ionic liquid at the n-type oxide/perovskite interface. *Adv. Energy Mater.* **10**, 1903231 (2020).
111. Wu, Q. et al. Solution-processable ionic liquid as an independent or modifying electron transport layer for high-efficiency perovskite solar cells. *ACS Appl. Mater. Interfaces* **8**, 34464–34473 (2016).
112. Chen, W., Qi, D., Gao, X. & Wee, A. T. S. Surface transfer doping of semiconductors. *Prog. Surf. Sci.* **84**, 279–321 (2009).
113. Strobel, P., Riedel, M., Ristein, J. & Ley, L. Surface transfer doping of diamond. *Nature* **430**, 439–441 (2004).
114. Chen, W., Chen, S., Dong, C. Q., Xing, Y. G. & Wee, A. T. S. Surface transfer p-type doping of epitaxial graphene. *J. Am. Chem. Soc.* **129**, 10418–10422 (2007).
115. Rietwyk, K. J. et al. Charge transfer doping of silicon. *Phys. Rev. Lett.* **112**, 155502 (2014).
116. Gao, W. Y. & Kahn, A. Electrical doping: the impact on interfaces of pi-conjugated molecular films. *J. Phys. Condens. Matter* **15**, S2757–S2770 (2003).
117. Perry, E. E., Labram, J. G., Venkatesan, N. R., Nakayama, H. & Chabinyc, M. L. N-type surface doping of $MAPbI_3$ via charge transfer from small molecules. *Adv. Electron. Mater.* **4**, 1800087 (2018).
118. Noel, N. et al. Interfacial charge-transfer doping of metal halide perovskites for high performance photovoltaics. *Energy Environ. Sci.* **12**, 3063 (2019).
119. Arramel et al. Surface molecular doping of all-inorganic perovskite using zethrenes molecules. *Nano Res.* **12**, 77–84 (2019).
120. Lüssem, B., Riede, M. & Leo, K. Doping of organic semiconductors. *Phys. Status Solidi Appl. Mater. Sci.* **210**, 9–43 (2013).
121. Walzer, K., Maennig, B., Pfeiffer, M. & Leo, K. Highly efficient organic devices based on electrically doped transport layers. *Chem. Rev.* **107**, 1233–1271 (2007).
122. Yang, Y. et al. Low surface recombination velocity in solution-grown $CH_3NH_3PbBr_3$ perovskite single crystal. *Nat. Commun.* **6**, 7961 (2015).
123. Wu, B. et al. Long minority-carrier diffusion length and low surface-recombination velocity in inorganic lead-free $CsSnI_3$ perovskite crystal for solar cells. *Adv. Funct. Mater.* **27**, 1604818 (2017).

124. Jiang, Q. et al. Interfacial molecular doping of metal halide perovskites for highly efficient solar cells. *Adv. Mater.* **32**, 2001581 (2020).
125. Wu, W. et al. Molecular doping enabled scalable blading of efficient hole-transport-layer-free perovskite solar cells. *Nat. Commun.* **9**, 1625 (2018).
126. Liu, C. et al. Grain boundary modification via F4TCNQ to reduce defects of perovskite solar cells with excellent device performance. *ACS Appl. Mater. Interfaces* **10**, 1909–1916 (2018).
127. Chen, H. et al. Organic N-type molecule: Managing the electronic states of bulk perovskite for high-performance photovoltaics. *Adv. Funct. Mater.* **30**, 2001788 (2020).
128. Gaulding, E. A. et al. Conductivity tuning via doping with electron donating and withdrawing molecules in perovskite $CsPbI_3$ nanocrystal films. *Adv. Mater.* **31**, 1902250 (2019).
129. Heaney, M. B. in *Electrical Measurement, Signal Processing, and Displays* (ed. Webster, J. G.) (CRC, 2003).
130. Schroder, D. K. *Semiconductor Material And Device Characterization* (Wiley, 2006).
131. Zhang, Y. et al. Thermoelectric properties of all-inorganic perovskite $CsSnBr_3$: A combined experimental and theoretical study. *Chem. Phys. Lett.* **754**, 137637 (2020).
132. Zheng, L. et al. Enhanced thermoelectric performance of F4-TCNQ doped $FASnI_3$ thin films. *J. Mater. Chem. A* **8**, 25431–25442 (2020).
133. Liu, C. et al. Sn-based perovskite for highly sensitive photodetectors. *Adv. Sci.* **6**, 1900751 (2019).
134. Kirchartz, T. et al. Sensitivity of the Mott–Schottky analysis in organic solar cells. *J. Phys. Chem. C* **116**, 7672–7680 (2012).
135. Awni, R. A. et al. Influence of charge transport layers on capacitance measured in halide perovskite solar cells. *Joule* **4**, 644–657 (2020).
136. Almora, O., Aranda, C., Mas-Marzá, E. & Garcia-Belmonte, G. On Mott-Schottky analysis interpretation of capacitance measurements in organometal perovskite solar cells. *Appl. Phys. Lett.* **109**, 173903 (2016).
137. Gunawan, O. et al. Carrier-resolved photo-Hall effect. *Nature* **575**, 151–155 (2019).
138. Chen, Y. et al. Extended carrier lifetimes and diffusion in hybrid perovskites revealed by Hall effect and photoconductivity measurements. *Nat. Commun.* **7**, 12253 (2016).
139. Gunawan, O., Virgus, Y. & Tai, K. F. A parallel dipole line system. *Appl. Phys. Lett.* **106**, 062407 (2015).
140. Béchu, S., Ralaiarisoa, M., Etcheberry, A. & Schulz, P. Photoemission spectroscopy characterization of halide perovskites. *Adv. Energy Mater.* **10**, 1904007 (2020).
141. Cahen, D. & Kahn, A. Electron energetics at surfaces and interfaces: Concepts and experiments. *Adv. Mater.* **15**, 271–277 (2003).
142. Zhang, F. et al. Ultraviolet photoemission spectroscopy and Kelvin probe measurements on metal halide perovskites: Advantages and pitfalls. *Adv. Energy Mater.* **10**, 1903252 (2020).
143. Kahn, A. Fermi level, work function and vacuum level. *Mater. Horiz.* **3**, 7–10 (2016).
144. Hu, Z. et al. The impact of atmosphere on energetics of lead halide perovskites. *Adv. Energy Mater.* **10**, 2000908 (2020).
145. Gao, W. & Kahn, A. Electronic structure and current injection in zinc phthalocyanine doped with tetrafluorotetracyanoquinodimethane: Interface versus bulk effects. *Org. Electron.* **3**, 53–63 (2002).
146. Gao, W. & Kahn, A. Controlled *p* doping of the hole-transport molecular material N,N′-diphenyl-N,N′-bis(1-naphthyl)-1,1′-biphenyl-4,4′-diamine with tetrafluorotetracyanoquinodimethane. *J. Appl. Phys.* **94**, 359–366 (2003).
147. Dai, A. et al. Enhanced charge-carrier injection and collection via lamination of doped polymer layers p-doped with a solution-processible molybdenum complex. *Adv. Funct. Mater.* **24**, 2197–2204 (2014).
148. Herrbach, J., Revaux, A., Vuillaume, D. & Kahn, A. P-doped organic semiconductor: Potential replacement for PEDOT:PSS in organic photodetectors. *Appl. Phys. Lett.* **109**, 073301 (2016).
149. Méndez, H. et al. Charge-transfer crystallites as molecular electrical dopants. *Nat. Commun.* **6**, 8560 (2015).
150. Chappell, J. S. et al. Degree of charge transfer in organic conductors by infrared Absorption spectroscopy. *J. Am. Chem. Soc.* **103**, 2442–2443 (1981).
151. Goldstein, J. I. et al. *SEM Microscopy and X-Ray Microanalysis* (Springer, 2018).
152. Hoque, M. N. F., He, R., Warzywoda, J. & Fan, Z. Effects of moisture based grain boundary passivation on cell performance and ionic migration in organic–inorganic halide perovskite solar cells. *ACS Appl. Mater. Interfaces* **10**, 30322–30329 (2018).
153. Euvrard, J. et al. The formation of polymer-dopant aggregates as a possible origin of limited doping efficiency at high dopant concentration. *Org. Electron.* **53**, 135–140 (2018).
154. Harvey, S. P. et al. Probing perovskite inhomogeneity beyond the surface: TOF-SIMS analysis of halide perovskite photovoltaic devices. *ACS Appl. Mater. Interfaces* **10**, 28541–28552 (2018).
155. Atkin, J. M., Berweger, S., Jones, A. C. & Raschke, M. B. Nano-optical imaging and spectroscopy of order, phases, and domains in complex solids. *Adv. Phys.* **61**, 745–842 (2012).
156. Kubicki, D. J., Prochowicz, D., Pinon, A. & Stevanato, G. Doping and phase segregation in Mn^{2+} and Co^{2+} doped lead halide perovskites from ^{133}Cs and ^{1}H NMR relaxation enhancement. *J. Mater. Chem. A* **7**, 2326–2333 (2019).
157. Olthof, S. et al. Ultralow doping in organic semiconductors: Evidence of trap filling. *Phys. Rev. Lett.* **109**, 176601 (2012).
158. Peng, J., Chen, Y., Zheng, K., Pullerits, T. & Liang, Z. Insights into charge carrier dynamics in organo-metal halide perovskites: From neat films to solar cells. *Chem. Soc. Rev.* **46**, 5714–5729 (2017).
159. Savenije, T. J., Guo, D., Caselli, V. M. & Hutter, E. M. Quantifying charge-carrier mobilities and recombination rates in metal halide perovskites from time-resolved microwave photoconductivity measurements. *Adv. Energy Mater.* **10**, 1903788 (2020).
160. Linford, M. R. et al. Proliferation of faulty materials data analysis in the literature. *Microsc. Microanal.* **26**, 1–2 (2020).
161. Baer, D. R. & Gilmore, I. S. Responding to the growing issue of research reproducibility. *J. Vac. Sci. Technol. A* **36**, 068502 (2018).
162. Liao, J., Wu, W., Jiang, Y. & Zhong, J. Understanding of carrier dynamics, heterojunction merits and device physics: towards designing efficient carrier transport layer-free perovskite solar cells. *Chem. Soc. Rev.* **49**, 354–381 (2020).
163. Zhao, L. et al. Redox chemistry dominates the degradation and decomposition of metal halide perovskite optoelectronic devices. *ACS Energy Lett.* **1**, 595–602 (2016).
164. Sanehira, E. M. et al. Influence of electrode interfaces on the stability of perovskite solar cells: Reduced degradation using MoOx/Al for hole collection. *ACS Energy Lett.* **1**, 38–45 (2016).
165. Kato, Y. et al. Silver iodide formation in methyl ammonium lead iodide perovskite solar cells with silver top electrodes. *Adv. Mater. Interfaces* **2**, 1500195 (2015).
166. Calado, P. & Barnes, P. R. F. Is it possible for a perovskite p-n homojunction to persist in the presence of mobile ionic charge? Preprint at *ArXiv* 1905.11892 (2019).
167. Kirchartz, T. & Cahen, D. Minimum doping densities for p–n junctions. *Nat. Energy* **5**, 973–975 (2020).
168. Eames, C. et al. Ionic transport in hybrid lead iodide perovskite solar cells. *Nat. Commun.* **6**, 7497 (2015).
169. Game, O. S., Buchsbaum, G. J., Zhou, Y., Padture, N. P. & Kingon, A. I. Ions matter: Description of the anomalous electronic behavior in methylammonium lead halide perovskite devices. *Adv. Funct. Mater.* **27**, 1606584 (2017).
170. Chattopadhyay, D. & Queisser, H. J. Electron scattering by ionized impurities in semiconductors. *Rev. Mod. Phys.* **53**, 745–768 (1981).
171. Zhao, T., Shi, W., Xi, J., Wang, D. & Shuai, Z. Intrinsic and extrinsic charge transport in $CH_3NH_3PbI_3$ perovskites predicted from first-principles. *Sci. Rep.* **6**, 19968 (2016).
172. Filippetti, A., Mattoni, A., Caddeo, C., Saba, M. I. & Delugas, P. Low electron-polar optical phonon scattering as a fundamental aspect of carrier mobility in methylammonium lead halide $CH_3NH_3PbI_3$ perovskites. *Phys. Chem. Chem. Phys.* **18**, 15352–15362 (2016).
173. Wright, A. D. et al. Electron–phonon coupling in hybrid lead halide perovskites. *Nat. Commun.* **7**, 11755 (2016).
174. Sendner, M. et al. Optical phonons in methylammonium lead halide perovskites and implications for charge transport. *Mater. Horiz.* **3**, 613–620 (2016).
175. Wen, X. et al. Defect trapping states and charge carrier recombination in organic–inorganic halide perovskites. *J. Mater. Chem. C* **4**, 793–800 (2016).
176. Hutter, E. M., Gélvez-Rueda, M. C., Bartesaghi, D., Grozema, F. C. & Savenije, T. J. Band-like charge transport in $Cs_2AgBiBr_6$ and mixed antimony–bismuth $Cs_2AgBi_{1-x}Sb_xBr_6$ halide double perovskites. *ACS Omega* **3**, 11655–11662 (2018).
177. Stranks, S. D. et al. Recombination kinetics in organic-inorganic perovskites: excitons, free charge, and subgap states. *Phys. Rev. Appl.* **2**, 034007 (2014).
178. Shao, S. et al. The effect of the microstructure on trap-assisted recombination and light soaking phenomenon in hybrid perovskite solar cells. *Adv. Funct. Mater.* **26**, 8094–8102 (2016).
179. Zhang, Y., De Boer, B. & Blom, P. W. M. Trap-free electron transport in poly(*p*-phenylene vinylene) by deactivation of traps with *n*-type doping. *Phys. Rev. B Condens. Matter Mater. Phys.* **81**, 085201 (2010).
180. Lu, M. & Nicolai, H. T., . & Wetzelaer, G-J. A. H. & Blom, P. W. M. N-type doping of poly(p-phenylene vinylene) with air-stable dopants. *Appl. Phys. Lett.* **99**, 173302 (2011).
181. Qi, Y. et al. Solution doping of organic semiconductors using air-stable n-dopants. *Appl. Phys. Lett.* **100**, 083305 (2012).
182. Olthof, S. et al. Passivation of trap states in unpurified and purified C_{60} and the influence on organic field-effect transistor performance. *Appl. Phys. Lett.* **101**, 253303 (2012).
183. Tietze, M. L., Pahner, P., Schmidt, K., Leo, K. & Lüssem, B. Doped organic semiconductors: Trap-filling, impurity saturation, and reserve regimes. *Adv. Funct. Mater.* **25**, 2701–2707 (2015).
184. Higgins, A., Mohapatra, S. K., Barlow, S., Marder, S. R. & Kahn, A. Dopant controlled trap-filling and conductivity enhancement in an electron-transport polymer. *Appl. Phys. Lett.* **106**, 163301 (2015).
185. Milot, R. L. et al. Radiative monomolecular recombination boosts amplified spontaneous emission in $HC(NH_2)_2SnI_3$ perovskite films. *J. Phys. Chem. Lett.* **7**, 4178–4184 (2016).
186. Miller, S. A. et al. Empirical modeling of dopability in diamond-like semiconductors. *npj Comput. Mater.* **4**, 71 (2018).
187. Zhang, S. B., Wei, S. H. & Zunger, A. A phenomenological model for systematization and prediction of doping limits in II–VI and I–III–VI_2 compounds. *J. Appl. Phys.* **83**, 3192–3196 (1998).
188. Yang, J. H. et al. Enhanced p-type dopability of P and As in CdTe using non-equilibrium thermal processing. *J. Appl. Phys.* **118**, 025102 (2015).
189. Yang, J. H. et al. Tuning the Fermi level beyond the equilibrium doping limit through quenching: The case of CdTe. *Phys. Rev. B Condens. Matter Mater. Phys.* **90**, 245202 (2014).
190. Rakita, Y., Lubomirsky, I. & Cahen, D. When defects become 'dynamic': halide perovskites: a new window on materials? *Mater. Horiz.* **6**, 1297–1305 (2019).
191. Kumar, S., Hodes, G. & Cahen, D. Defects in halide perovskites: The lattice as a boojum *? *MRS Bull.* **45**, 478–484 (2020).
192. Zhao, L., Lin, Y. L., Kim, H., Giebink, N. C. & Rand, B. P. Donor/acceptor charge-transfer states at two-dimensional metal halide perovskite and organic semiconductor interfaces. *ACS Energy Lett.* **3**, 2708–2712 (2018).
193. Gélvez-Rueda, M. C. et al. Inducing charge separation in solid-state two-dimensional hybrid perovskites through the incorporation of organic charge-transfer complexes. *J. Phys. Chem. Lett.* **11**, 824–830 (2020).
194. Cui, P. et al. Highly efficient electron-selective layer free perovskite solar cells by constructing effective p–n heterojunction. *Sol. RRL* **1**, 1600027 (2017).
195. Stoumpos, C. C., Malliakas, C. D. & Kanatzidis, M. G. Semiconducting tin and lead iodide perovskites with organic cations: Phase transitions, high mobilities, and near-infrared photoluminescent properties. *Inorg. Chem.* **52**, 9019–9038 (2013).
196. Wei, H. et al. Dopant compensation in alloyed $CH_3NH_3PbBr_{3-x}Cl_x$ perovskite single crystals for gamma-ray spectroscopy. *Nat. Mater.* **16**, 826–833 (2017).

197. Dang, Y. et al. Formation of hybrid perovskite tin iodide single crystals by top-seeded solution growth. *Angew. Chem. Int. Ed.* **55**, 3447–3450 (2016).
198. Chan, C. K. et al. N-type doping of an electron-transport material by controlled gas-phase incorporation of cobaltocene. *Chem. Phys. Lett.* **431**, 67–71 (2006).
199. Lee, D. H. et al. Simultaneous enhancement of charge density and molecular stacking order of polymer semiconductors by viologen dopants for high performance organic field-effect transistors. *J. Mater. Chem. C* **6**, 5497–5505 (2018).
200. Zhang, F. & Kahn, A. Investigation of the high electron affinity molecular dopant F6-TCNNQ for hole-transport materials. *Adv. Funct. Mater.* **28**, 1703780 (2018).
201. Qi, Y. et al. Use of a high electron-affinity molybdenum dithiolene complex to p-dope hole-transport layers. *J. Am. Chem. Soc.* **131**, 12530–12531 (2009).
202. Belasco, J. et al. Molecular doping and tuning threshold voltage in 6,13-bis(triisopropylsilylethynyl) pentacene/polymer blend transistors. *Appl. Phys. Lett.* **105**, 063301 (2014).
203. Endres, J. et al. Valence and conduction band densities of states of metal halide perovskites: A combined experimental-theoretical study. *J. Phys. Chem. Lett.* **7**, 2722–2729 (2016).
204. Schulz, P. et al. Interface energetics in organo-metal halide perovskite-based photovoltaic cells. *Energy Environ. Sci.* **7**, 1377–1381 (2014).

Acknowledgements
The authors thank A. Kahn for the helpful discussions. J.E. and D.B.M. are supported by the National Science Foundation under grant no. 1709294. Y.Y. acknowledges support from the Center for Hybrid Organic-Inorganic Semiconductors for Energy (CHOISE), an Energy Frontier Research Center funded by the Office of Basic Energy Sciences, Office of Science within the U.S. Department of Energy through contract number DE-AC36-08G028308.

Author contributions
All authors contributed to the discussion of content. J.E. researched the data and wrote the initial draft. D.B.M. and Y.Y. revised the manuscript.

Competing interests
The authors declare no competing interests.

Publisher's note
Springer Nature remains neutral with regard to jurisdictional claims in published maps and institutional affiliations.

© Springer Nature Limited 2021